FINAL REPORT

A Novel Reactive Electrochemical Membrane System for Treatment of Mixed Contaminants

SERDP Project ER-2717

JANUARY 2019

Qingguo Huang
University of Georgia

SERDP
DOD ▪ EPA ▪ DOE

Page Intentionally Left Blank

Page Intentionally Left Blank

REPORT DOCUMENTATION PAGE

Form Approved
OMB No. 0704-0188

1. REPORT DATE *(DD-MM-YYYY)*	2. REPORT TYPE	3. DATES COVERED *(From - To)*
01/31/2019	SERDP Final Report	6/20/2017 - 6/19/2019

4. TITLE AND SUBTITLE
A Novel Reactive Electrochemical Membrane System for Treatment of Mixed Contaminants

5a. CONTRACT NUMBER
17-C-0010

5b. GRANT NUMBER

5c. PROGRAM ELEMENT NUMBER

6. AUTHOR(S)
Qingguo Huang

5d. PROJECT NUMBER
ER-2717

5e. TASK NUMBER

5f. WORK UNIT NUMBER

7. PERFORMING ORGANIZATION NAME(S) AND ADDRESS(ES)
University of Georgia
1109 Experiment St, Room 272 Redding Bldg
Griffin, GA 30223

8. PERFORMING ORGANIZATION REPORT NUMBER
ER-2717

9. SPONSORING/MONITORING AGENCY NAME(S) AND ADDRESS(ES)
Strategic Environmental Research and Development Program
4800 Mark Center Drive, Suite 17D03
Alexandria, VA 22350-3605

10. SPONSOR/MONITOR'S ACRONYM(S)
SERDP

11. SPONSOR/MONITOR'S REPORT NUMBER(S)
ER-2717

12. DISTRIBUTION/AVAILABILITY STATEMENT
DISTRIBUTION A. Approved for public release: distribution unlimited.

13. SUPPLEMENTARY NOTES

14. ABSTRACT
The aim of this limited scope project was to prove the concept of using a reactive electrochemical membrane (REM) system to remove and degrade mixed Contaminants of Concerns (CoCs) in groundwater. The REM system involves an electric-conductive porous Magnéli phase titanium sub-oxide ceramic material that serves simultaneously as a three-dimensional (3-D) anode and a membrane through which contaminant-containing water is filtered and treated electrochemically.

15. SUBJECT TERMS
Novel Reactive Electrochemical Membrane System, Treatment, Mixed Contaminants

16. SECURITY CLASSIFICATION OF:			17. LIMITATION OF ABSTRACT	18. NUMBER OF PAGES	19a. NAME OF RESPONSIBLE PERSON
a. REPORT	b. ABSTRACT	c. THIS PAGE			Qingguo Huang
UNCLASS	UNCLASS	UNCLASS	UNCLASS		19b. TELEPHONE NUMBER *(Include area code)* 770-229-3302

Page Intentionally Left Blank

Table of Content

Abstract

Introduction and Objectives

The aim of this limited scope project was to prove the concept of using a reactive electrochemical membrane (REM) system to remove and degrade mixed Contaminants of Concerns (CoCs) in groundwater. The REM system involves an electric-conductive porous Magnéli phase titanium sub-oxide ceramic material that serves simultaneously as a three-dimensional (3-D) anode and a membrane through which contaminant-containing water is filtered and treated electrochemically.

Per- and polyfluoroalkyl substances (PFAS) are the major target CoCs of this study, with a focus on the most persistent perfluoroalkyl acids (PFAAs). The occurrence of PFAS in the environment is widespread and has caused serious concerns. PFASs, in particular PFAAs, are toxic and extremely persistent, posing challenges to treatment technologies for their degradation. Our recent study indicated that PFAAs may be effectively degraded by electrooxidation using Magneli phase titanium sub-oxides (TSO) as anodes. Magneli phase TSO are a series of substoichiometric titanium oxides with the formula of Ti_nO_{2n-1}. This study was conducted to probe the hypothesis that the EO performance on PFAA degradation will be enhanced with porous TSO ceramic anodes used in REM systems than in batch reactors under similar electrochemical conditions.

Technical Approach

Three different types of porous TSO ceramic anodes were fabricated by a high-temperature sintering method from Ti_4O_7 powders of nanometer sizes or micrometer sizes, including circular nano-Ti_4O_7, circular micro-Ti_4O_7 or rectangular nano-Ti_4O_7 anodes, named according to their shape and the size of the Ti_4O_7 particles used for fabrication. A commercially available type of Ebonex tubular anodes was also tested in this study. The X-ray diffraction (XRD) spectroscopy indicated that the three types of anodes fabricated in house were primarily composed of Ti_4O_7, while the main component of Ebonex was determined to be Ti_9O_{17}. Mercury intrusion porosimetry revealed the differences in porous structure among the four anode materials studied in this project.

Experiments were performed to evaluate electrooxidation (EO) treatment efficiency of the four different types of anodes in batch reactors on solutions containing only PFOS or a mixture of PFAAs, including PFBA, PFPeA, PFHxA, PFHpA, PFOA, PFBS, PFHxS and PFOS, as model contaminants. The tests were conducted under different operation conditions, in an attempt to compare the treatment efficiency of different anodes and the effects of major operation parameters, water compositions and co-contaminants. Batch EO treatment experiments were also performed to evaluate the formation of chlorate and perchlorate during PFOS degradation in the presence of Cl^- and compared with that on the boron doped diamond (BDD) anode. Based on the results of EO treatment in batch reactors, we have further evaluated two TSO anodes, circular nano-Ti_4O_7 and Ebonex, in a series of REM treatments operated in cross-flow filtration mode with solutions containing PFOS only or the PFAA mixture.

Results

Degradation of all PFAAs was observed in the experiments performed to evaluate electrooxidation (EO) treatment efficiency of all four different types of anodes, with near stoichiometric formation of F^- in systems that have been tested for fluoride release. Increase in current density resulted in more efficient PFAA degradation, likely because of the increased anodic potential. It appeared that

the EO performance in degrading PFAAs was dependent on the composition of the anode material and their pore structure. The three Ti_4O_7 anodes exhibited much greater performance than that of the Ebonex that is mainly composed of Ti_9O_{17}. These are also reflected by their energy consumption per log reduction of PFOS (EE/O) which was much higher for the Ebonex anode than the other three anodes. The three Ti_4O_7 anodes also exhibited some difference in terms of EO reactivity towards PFAA, likely related to the difference in pore structure among the three anodes that can in turn impact mass transfer and electric potential distribution on the anode surface. The pseudo-first order reaction rate constant normalized by anode surface area (k_{SA}) for PFAA in the mixture was not much different from that obtained when each PFAA was spiked in the solution individually, indicating the absence of strong competitive effect among the PFAAs in the mixture under the experiment conditions.

The change in electrolyte type, concentration and pH of the reaction solution appeared to have minimal if any impact on PFOS degradation during EO treatment by TSO anodes. This is probably because the bulk solution conditions may have very little effect on the anode surface conditions that are controlled by the water oxidation reactions on the anode at our experiment conditions. The presence of trichloroethylene (TCE) in the reaction solution was also tested, and appeared to have very limited impact on PFOS degradation during EO treatment.

Batch EO treatment experiments were also performed to evaluate the formation of chlorate and perchlorate during PFOS degradation on rectangular nano-Ti_4O_7 anode in the presence of Cl^- and compared with that on the boron doped diamond (BDD) anode. It showed that the formation of chlorate and perchlorate was much slower on the Ti_4O_7 anode than on the BDD anode. This is because the oxidation of Cl^- due to direct electron transfer (DET) on Ti_4O_7 anode did not occur as opposed to BDD. The slow rates of chlorate and perchlorate formation on Ti_4O_7 anode is an advantage for application of this type of anodes in water treatment.

Based on the results of EO treatment in batch reactors, we have further evaluated two TSO anodes, circular nano-Ti_4O_7 and Ebonex, in a series of REM treatments operated in cross-flow filtration mode with solutions containing PFOS only or the PFAA mixture. Effective PFAA degradation was found on both anodes, and the nano-Ti_4O_7 REM exhibited better performance on PFOS removal than the Ebonex REM at the same anodic potential. PFAA removal rate increased with increasing current density, consistent with that observed for batch reactor treatment. PFAA degradation rate was greatly higher in the REM treatment than in the batch reactor treatment for the same anode, as indicated by reaction rate constant normalized to the active electrochemical surface area. Accordingly, the electrical energy required to reduce the PFOS concentration by one order of magnitude (EE/O) by REM was much lower than that of the batch reactor treatment. The results indicated that REM enhanced EO efficiency not only by increasing substrate interphase mass transfer rates via convection facilitated dispersion but also making more anode surface available for reaction with the solution filtered through the REM.

The results of the experiments of REM treatment on the PFAA mixture indicated that, in general, the long-chain PFAA degraded more effectively than the shorter chain ones. The order of the degradation rate constants for the PFAAs differ between the REM and the batch reactor treatments, with the degradation of PFCAs becoming faster than that of PFSAs in REM as opposed to that in the batch reactor. Chlorate and perchlorate were formed in the permeate during REM treatment of PFAA solutions in the presence of chloride, dependent on the applied current density, but their formation appeared to be at lower levels than that in batch reactor, probably because of the much

shorter residence time in the membrane during REM. Control of chlorate and perchlorate formation by regulating EO conditions and other means is possible and worth of further study.

Benefits

Results of this study indicated that electrooxidation based on TSO membrane anodes is effective in degrading PFAAs and that REM mode led to significantly higher PFAA degradation efficiency with much lower energy consumption than the batch mode. The TSO-based electrooxidation in REM mode provides an innovative scheme potentially promising for PFAS treatment. This scheme offer not only effective PFAA degradation but also minimized chlorinated byproduct formation. The treatment performance is not dependent on water compositions and can thus be applied to complex wastewaters with co-contaminants. In addition, the electrooxidation approach has multiple advantages in general, including no need of chemical additions and ease for modular and automated operations. Compared to boron doped diamond anodes, the TSO anodes can be fabricated at lower costs and larger measures.

It is envisioned that such TSO-based REM technology may be used to treat PFAS in contaminated groundwater in pump-and-treat scenarios such as what is schematically represented in the below figure. A more systematic study is needed to provide a basis for design and optimization of the REM systems for applications on sites to remediate PFAS contamination, including 1) to further examine the performance of REM systems on a wide range of per- and polyfluoroalkyl substances (PFAS) under various operation conditions; 2) to modify the titanium suboxide materials used in the REM as membranes for improved performances and minimized reactivity towards chloride; and 3) to examine the feasibility of the REM systems for in-situ and pump-and-treat application scenarios using real water and soil samples from contaminated sites.

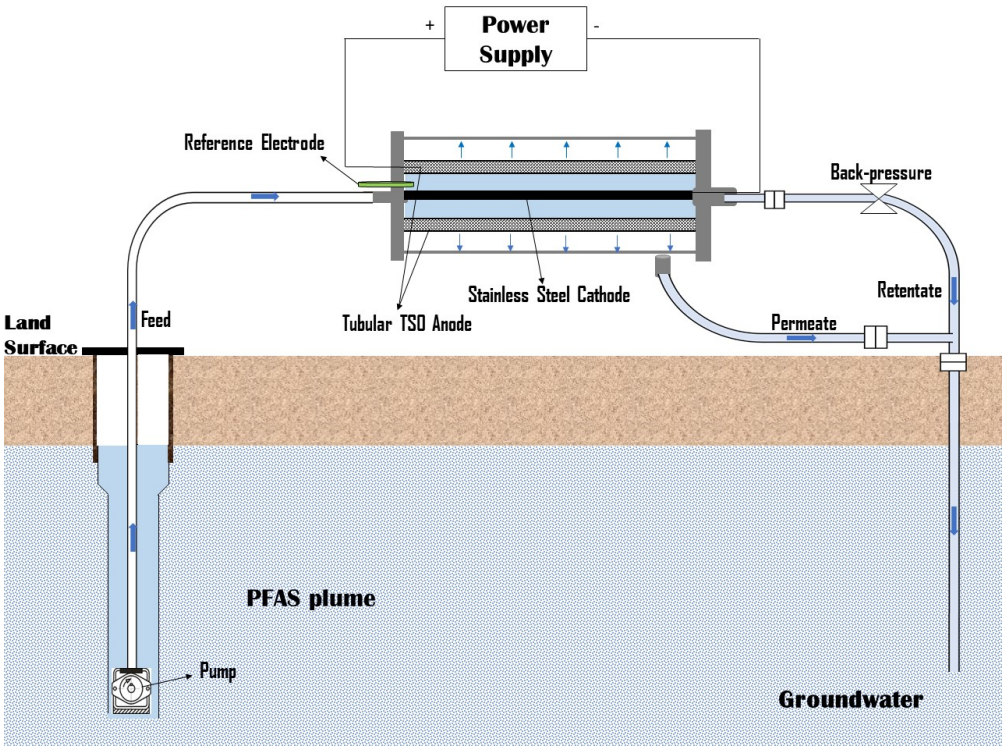

1. Introduction

This project aimed to prove the concept of a novel treatment scheme involving a reactive electrochemical membrane (REM) system to remove and degrade mixed Contaminants of Concerns (CoCs) in groundwater. Per- and polyfluoroalkyl substances (PFAS) are the major target CoCs to be studied in this project, with a focus on the most persistent perfluoroalkyl acids (PFAAs). The influence of trichloroethylene (TCE) as a co-existing contaminant was also tested. The REM system involves an electric-conductive porous ceramic membrane that serves simultaneously as a three-dimensional (3-D) anode and a membrane through which contaminant-containing water is filtered and treated electrochemically. The anodes to be examined focuses on the Magnéli phase titanium sub-oxide ceramic materials, including Ti_4O_7 and a commercially available Ebonex material.

Magneli phase titanium sub-oxides (TSO) are a series of substoichiometric titanium oxides with the formula of Ti_nO_{2n-1}, such as Ti_4O_7, Ti_5O_9, Ti_6O_{11}, which have recently been explored as promising candidates for electrochemical applications because of their high conductivity, chemical inertness, and low cost of production (Lindstrom et al. 2011, Zaky and Chaplin 2013). TSO can serve as an ideal electrode in electrochemical wastewater treatment. Studies have shown that TSO behaves as typical "non-active" electrodes and thus produces hydroxyl free radicals (·OH) via water oxidation, and is also active for direct electron transfer reactions, which thus promotes PFOA/PFOS electron transfer and subsequent complete mineralization (Liang 2018, Lin et al. 2018, Niu et al. 2012). Among all TSO materials, Ti_4O_7 exhibits the best conductivity and electrochemical properties (Lin et al. 2018).

This report summarizes the results of our project and is organized in four sections (2-5). Section 2 describes the activities in material fabrication and characterization. Section 3 summarizes the results of EO treatment in batch reactor using titanium suboxide anode. The results of experiments with PFOS spiked as an individual model contaminant was presented in Section 3.2 as a benchmark for comparison of different TSO materials, and the results of a mixture of 8 PFAAs was shown in Section 3.3. The study results on REM treatments in cross-flow filtration mode are summarized in section 4. Section 5 briefly introduces future plans.

2. Material fabrication and characterization

2.1 Material fabrication

A high-temperature sintering method was used to fabricate the porous titanium suboxide (TSO) anodes to be used in REM systems. First, TSO powders were produced by reducing TiO_2 powders at high temperature (950 °C) under controlled H_2 atmosphere. The TiO_2 powders of two different sizes, one of nanometer scale and the other in micrometer range, have been used, and two TSO powders were thus obtained, with one having diameters in the range of 1-3 nm and the other having diameters in the range of 0.8-2.0 μm. They were characterized by X ray diffraction (XRD) spectroscopy and found to be primarily composed of Ti_4O_7. The Ti_4O_7 powders of the nanometer sizes were used to prepare ceramic electrodes of two different shapes by sintering, a circular shape (25 mm diameter, 2 mm thickness) and a rectangular shape (100 mm × 50 mm ×2 mm), while the Ti_4O_7 powders of the micrometer sizes have also been used to make the circular shape electrode.

For making the rectangular electrode, the Ti_4O_7 nano powder were mixed with water and a binder (polyacrylamide and polyvinyl alcohol, 5 wt.% in mass ratio) to form a slurry. The slurry was then spray-dried to small granulates, which were then placed in a mold and pressed into a green-body (an unsintered ceramic item). After heated at 85 °C to burn off the binder, the green body was sintered at high temperature (900 °C) under vacuum (Liang 2018). For making the circular shape electrode, the Ti_4O_7 nano or micro powders were pressed in a customized mold, sintered at high temperature (1150 °C for the nano powder or 1100 °C for micro powder) under vacuum. According to the shape of the membranes and the particle size of the Ti_4O_7 powders used for sintering, the anodes used in this study were named as circular nano-Ti_4O_7, circular micro-Ti_4O_7 or rectangular nano-Ti_4O_7 anodes, respectively as indicated in Figure 1.

In addition, a so called Ebonex material in a tubular shape (length 100 mm, inner diameter 20 mm, outer diameter 28 mm) was obtained from Vector Corrosion Technologies, Inc. (Ontario, Canada), and tested as an anode in REM in this study. The Ebonex material is claimed to be a porous ceramic comprising TSO materials.

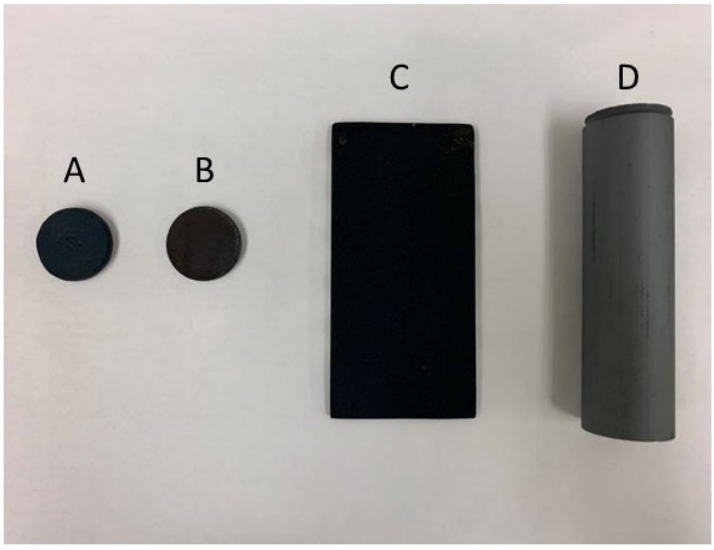

Figure 1. Anode materials: circular nano-Ti_4O_7 anode (A), circular micro-Ti_4O_7 anode (B), rectangular nano-Ti_4O_7 anode (C) and Ebonex anode (D).

2.2 Material characterization

All different types of anode materials were characterized by XRD and compared to that of standard reference materials to identify the composition and phases of the materials (Figure 2). The XRD pattern of the circular nano-Ti_4O_7, micro-Ti_4O_7, and rectangular nano-Ti_4O_7 are very similar to each other and all determined to be primarily composed of Ti_4O_7. The main component of Ebonex was determined to be Ti_9O_{17} by XRD.

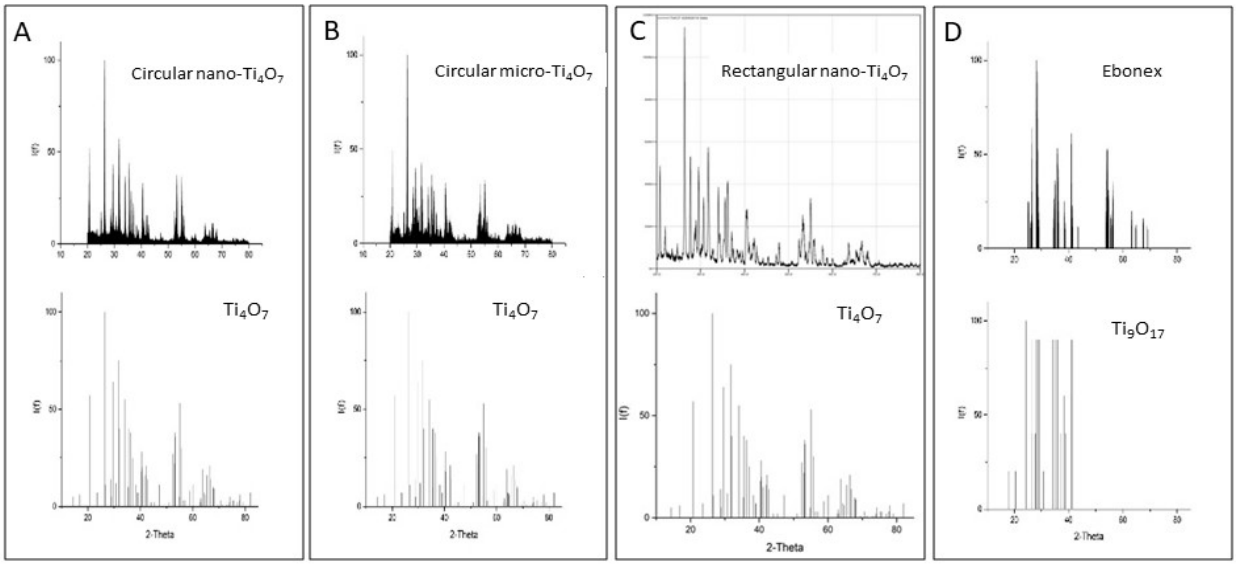

Figure 2. XRD results of circular nano-Ti_4O_7 (A), circular micro-Ti_4O_7 (B), rectangular nano-Ti_4O_7 (C) and Ebonex (D).

Mercury intrusion porosimetry was also performed to evaluate the porosity, pore size distribution and pore volume of all anode materials. The porosimetry analysis was conducted by Micrometric Analytical Services (Norcross, GA) according to method ISO 15901-1, and the results are summarized in Table 1, and the pore size distribution is displayed in Figure 3. A couple of interesting observations can be made from these results. The circular and rectangular nano-Ti_4O_7 materials, although both made from the same Ti_4O_7 nano powders, have pore structures of some difference. The circular nano-Ti_4O_7 material tends to have higher porosity (42.45 vs 34.90%), larger pore surface area (1.088 vs 0.308 m^2/g) and smaller pore sizes (1.17 vs 2.26 μm median pore size) than rectangular nano-Ti_4O_7 material. This is probably because the fabrication of rectangular anode involves a granulation process that was absent for making the circular anode. The circular micro-Ti_4O_7 material exhibits the highest porosity (59.84%) and pore surface area (8.25 m^2/g). Its pore size distribution (Figure 3B) shows that it has two types of pores, one in the micrometer range and the other in nanometer range, while the nanometer pores are not evident in the other three anode nanomaterials, except a small fraction of low nanometer pores seemingly present in the circular nano-Ti_4O_7 material. The nanopores in circular micro-Ti_4O_7 material has contributed to its porosity and pore surface area although its median pore size (1.31μm) is not significantly different from the other materials. The Ebonex material has the least porosity (17.29%), pore surface area (0.193 m^2/g), and median pore size (1.12 μm) among all four anode materials.

Table 1. Summary of porosimetry characterization on four anode materials

	Circular Nano-Ti_4O_7	**Rectangular Nano-Ti_4O_7**	**Circular Micro-Ti_4O_7**	**Ebonex**
Substance	Ti_4O_7	Ti_4O_7	Ti_4O_7	Mainly Ti_9O_{17}
Shape	Circular	Rectangular	Circular	Tubular
Size	Diameter: 25 mm	100 mm × 50 mm × 2 mm	Diameter: 25 mm	Inner diameter: 20 mm
	Thickness: 2 mm		Thickness: 2.0 mm	Outer diameter: 28 mm
				Length: 100 mm
Median pore diameter (μm)	1.17	2.26	1.31	1.12
Total pore area (m^2/g)	1.088	0.308	8.25	0.193
Porosity (%)	42.45	34.89	59.83	17.29

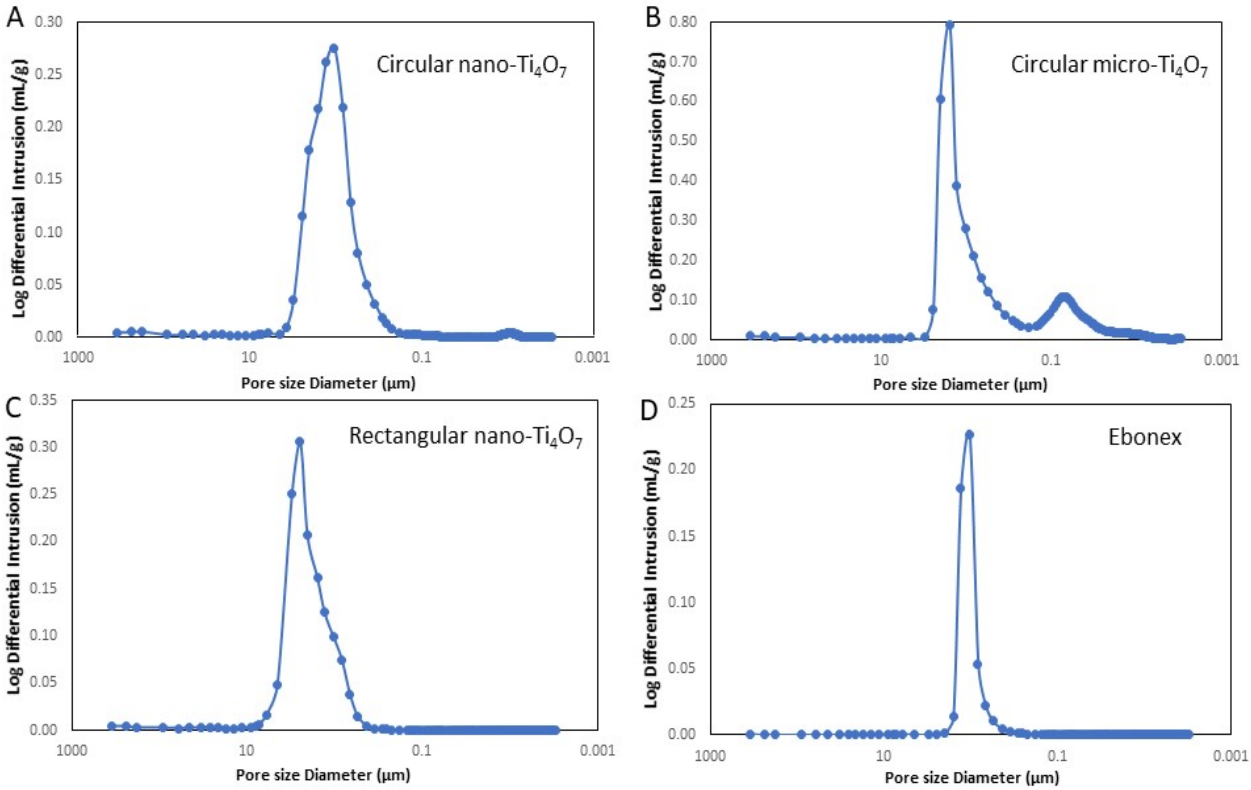

Figure 3. Results of mercury intrusion porosimetry analysis of pore size distribution: circular nano-Ti_4O_7 (A), circular micro-Ti_4O_7 (B), rectangular nano-Ti_4O_7 (C), and Ebonex (D).

3. Treatment in Batch Mode

A series of experiments have been conducted to examine the efficiency of EO treatment in batch reactors. Solutions with only PFOS spiked were tested as a model contaminant with different anode materials and under different key operation conditions, including current density, electrolytes and pH. The objective was to compare the treatment efficiency of different anodes and the effects of major operation parameters (Section 3.2). Experiments were also conducted to evaluate the performance of selected systems on a mixture of PFAAs including PFBA, PFPeA, PFHxA, PFHpA, PFOA, PFBS, PFHxS and PFOS (Section 3.3). The release of fluoride was also evaluated for selected systems and discussed in Section 3.4. Formation of chlorate and perchlorate when chloride was present in the system was evaluated in selected treatment conditions and discussed in Section 3.5.

3.1 Experiments

Four batch reactor setups have been employed according to the types of the anodes to be examined, with details described below (see Figure 4).

3.1.1 Reactor Setup

Reactor setup I was used to test the performance of the circular electrodes (25 mm diameter). The experiments were carried out in 70 mL polypropylene vessels, each containing 50 mL reaction solution having 2-μM PFOS in 100-mM Na_2SO_4 as the supporting electrolyte. A 316 stainless steel plate of the same size and shape was used as the cathode and placed in parallel to the anode at 2.5 cm gap. The effective anode surface area was 3.70 cm^2.

Reactor setup II was used for the rectangular anodes, comprising a 125 mL custom-made acrylic vessel with grooved slots to place electrodes. Two 316 stainless steel plates of the same size as the anode was used as cathodes that were placed in parallel to the anode on each side at 2.0 cm gap. The experiment was performed with 100 mL reaction solution in different electrolytes. The effective anode surface area was 32.90 cm^2.

Reactor setup III was similar to Reactor II, also used for rectangular anode, but had larger reaction volume. The reactor was 275-mL customized acrylic vessel with grooved slots for placing the rectangular electrodes. Two 316 stainless steel plates of the same size as the anode were used as cathodes that were placed in parallel to the anode on each side at 2.0 cm gap. The EO treatment experiments were carried with 200 mL reaction solution in 100 mM Na_2SO_4 as the supporting electrolyte. The effective surface area was 75.00 cm^2.

Reactor setup IV was used for testing the Ebonex anode. The reactor was a 275 mL customized acrylic vessel. A 316 stainless steel rod was used as the cathode that was placed in the middle of tubular reactor with its distance to the inner surface of anode to be 0.8 cm. The experiment was conducted either with 100 mL or 250 mL solution in 100-mM Na_2SO_4 as the supporting electrolyte. For 100-mL reaction volume, the effective surface area was 18.84 cm^2, while for 250 mL reaction volume, the effective surface area was 43.96 cm^2.

For all reactor setups, a 303 DM DC power supply (Electro Industries, USA) was used to provide electricity at varying current densities. The initial concentration of PFOS or a PFAA in the mixture was 2 μM in all cases unless otherwise specified. At prescribed time intervals, 400 μL sample was withdrawn from the reactor to analyze for PFAAs concentrations.

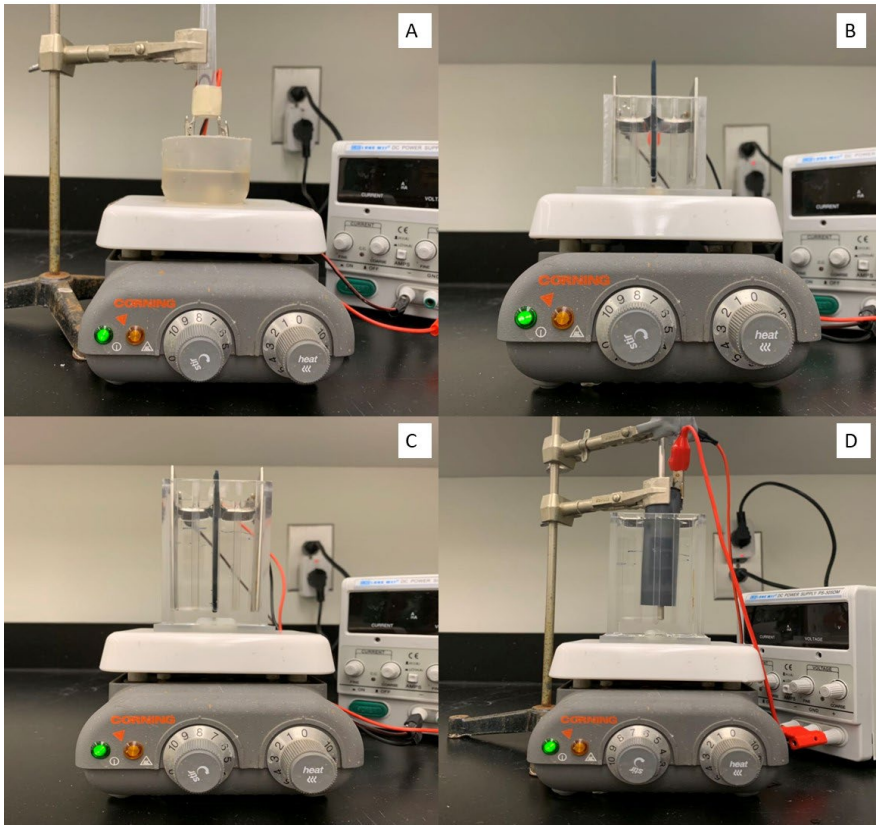

Figure 4. Batch reactor setup: Reactor setup I (A), Reactor setup II (B) and Reactor setup III (C) and Reactor setup IV (D).

3.1.2 Analytical methods

The 400 µL PFOS or mixture samples was first mixed with 400 µL methanol containing perfluoro-1-[$^{13}C_8$]-octane sulfonate (M8PFOS) as the internal standard. PFAS quantification was performed on an ultra-performance liquid chromatography coupled with a triple-stage quadrupole mass spectrometer (ACQUITY UPLC-MS/MS, Xevo TQD, Waters Corp., USA). an Acquity UPLC BEH C18 column (2.1 mm × 50 mm, 1.7 µm) was used for UPLC separation with a mobile phase consisting of a water solution containing 2-mM ammonium acetate (A) and methanol containing 2-mM ammonium acetate (B) at a flow rate of 0.3 mL/min: 30% A and 70% B for the entire program. Electrospray ionization was operated in a negative mode for PFAS detection with the parameters set as capillary voltage at 1.14 kV, cone voltage 60 V, desolvation temperature at 400 ºC, source block temperature at 100 ºC. Nitrogen (> 99.999% purity, Airgas) was used as the nebulizer and drying gas with the flow rates at 50 and 500 L/hour, respectively. Multiple reaction monitoring (MRM) was used to quantify PFAS and their isotope labeled standards at the transition *m/z* = 412.80 > 368.80 for PFOA, *m/z* = 498.70 > 80.00 for PFOS, and *m/z* = 507.00 > 80.00 for M8PFOS. In addition to PFOA and PFOS, additional PFAS that were also monitored, including the transitions *m/z* = 213.00 > 169.00 (perfluoro-n-butanoic acid, PFBA), *m/z* = 263.00 > 219.00 (perfluoro-n-pentanoic acid, PFPeA), *m/z* = 313.00 > 269.00 (perfluoro-n-hexanoic acid, PFHxA), *m/z* = 363.00 > 319.00 (perfluoro-n-heptanoic acid, PFHpA), *m/z* = 298.90 >79.90 (perfluoro-1-butanesulfonate, PFBS), *m/z* = 399.00 > 80.00 (perfluoro-1-hexanesulfonate, PFHxS).

Quantification of PFAS concentration was achieved by the ratio between PFAS and M8PFOS in reference to a five-point calibration curve. A list of the chemicals monitored in our analytical method is included in Appendix 2 with detection limits.

Anodic potential was measured using a CHI 660E electrochemical workstation (Austin, TX) with a leak-free Ag/AgCl reference electrode (Warner Instruments, LF-100), placed 0.85 mm from the anode surface.

Fluoride analysis was conducted by two methods. One method involved the use of chromatography (Dionex ICS-1100), with the mobile phase comprising a solution containing 15 mM KOH at a flow rate of 1.0 mL/min. The retention time for fluoride was 4.0 min (Luo et al. 2018). The other method involved the use of a used ion selective electrode (ISE) (Thermo Scientific^{TM} Orion^{TM}).

3.1.3 Reaction rate analysis

Based on the data of a substrate concentration collected over time, pseudo-first-order kinetic rate constant k of the substrate degradation was calculated for each reaction condition according to the following equation (1):

$$k = -ln\frac{C_t}{C_0} \times \frac{1}{t} \qquad (1)$$

where C_0 is the substrate concentration at time zero (mol/L); C_t is the substrate concentration (mol/L) at time t (s). To enable comparison between different electrodes, the surface area normalized reaction rate constant (k_{SA}) was calculated by the following equation (2):

$$k_{SA} = k \times \frac{V}{S} \qquad (2)$$

where V is the volume of the reaction solution (m^3); S the effective surface area of the anode (m^2).

3.2 Results: PFOS degradation

A number of experiments were conducted to evaluate the performance of EO treatment in batch mode on solutions having PFOS spiked as an individual model contaminant under varying conditions. The following factors and effects were evaluated, with the results summarized in Appendix 1 and each discussed in subsections below.

1. Anode materials and current densities.
2. Electrical efficiency per log order reduction (EE/O)
3. Electrolyte and pH
4. Impact of TCE

3.2.1 Impact of anode material and current density

The degradation of PFOS on the circular nano-Ti_4O_7 anode under different current densities is displayed in Figure 5 as an example to demonstrate the typical time-course profile of PFOS during EO treatment in a batch reactor. PFOS removal was not evident without current applied, but increased as the applied current density increased, with 2.0-μM PFOS completely eliminated after 20 minutes under 90 mA/cm^2 current density. F^- concentration was quantified in selected treatment systems and the results are summarized in Section 3.4. Near stoichiometric release of F^- has been observed as in previous reports on EO treatment of PFOS, providing a strong evidence of PFOS mineralization during EO treatment (Lin et al. 2018, Schaefer et al. 2015). Formation of shorter

chain PFAAs were not observed, except that only trace amounts of PFBA and PFPeA can be detected in systems with low current densities (below 5.0 mA/cm^2) at early reaction time (< 10 minutes). This is consistent with an earlier report, suggesting that PFOS tends to be completely mineralized on anode without significant intermediate release (Lin et al. 2018).

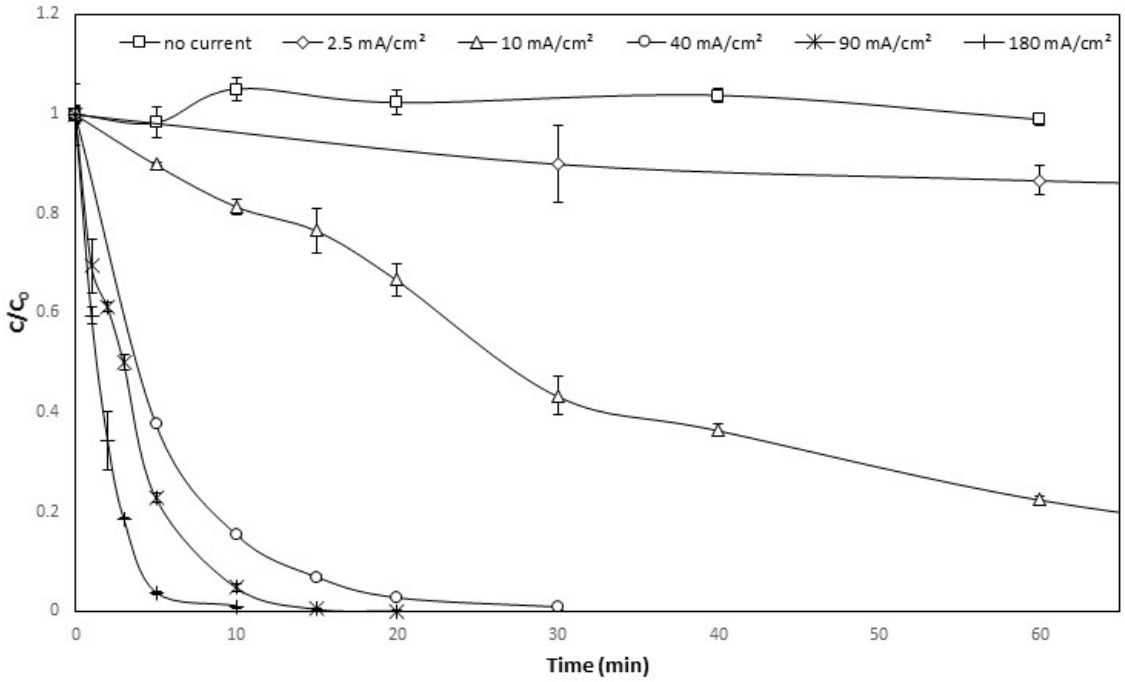

Figure 5. The concentration of L-PFOS during EO treatment of PFOS during EO in batch reactor with circular nano-Ti_4O_7 (Reactor I) at different current densities. Error bar represents standard deviation (n=3).

PFOS degradation in batch systems with different anodes under 40.0 mA/cm^2 are compared in Figure 6, as an example to demonstrate the impact of different anode materials on PFOS degradation. Both linear and branched PFOS (L-PFOS and B-PFOS) was quantified and shown in Figure 6A and 6B respectively. It should be noted that different anodes were tested in different reactor setups having different anode surface area to solution volume ratio. Therefore, PFOS degradation rate constant normalized to effective anode surface area (k_{SA}) was calculated to facilitate the comparison of reactivity across different anode materials and treatment conditions. Based on the data in Figure 6A, the k_{SA} of L-PFOS degradation was 3.88×10^{-4} m/s for circular nano-Ti_4O_7, 4.45×10^{-4} m/s for circular micro-Ti_4O, 3.43×10^{-4} m/s for rectangular nano-Ti_4O_7, and 8.30×10^{-5} m/s for the Ebonex anode. The three Ti_4O_7 anodes show similar reactivity, greater than that of Ebonex. The data of B-PFOS are shown in Figure 6B, based on which the k_{SA} of B-PFOS degradation was calculated to be 4.04×10^{-4}, 4.33×10^{-4}, 3.64×10^{-4}, and 8.52×10^{-5} for the circular nano-Ti_4O_7, circular micro-Ti_4O_7, rectangular nano-Ti_4O_7 and Ebonex anode respectively. They are either similar or slightly greater than those for L-PFOS. Because B-PFOS is composed only about 1/8 of the PFOS sample used in this study, and they comprise different isomers (branched at different sites) that are not completely resolved in UPLC. Therefore, the subsequent discussion on k_{SA}will focus on L-PFOS, although the k_{SA} for B-PFOS has also been calculated and listed in Appendix along with that of L-PFOS.

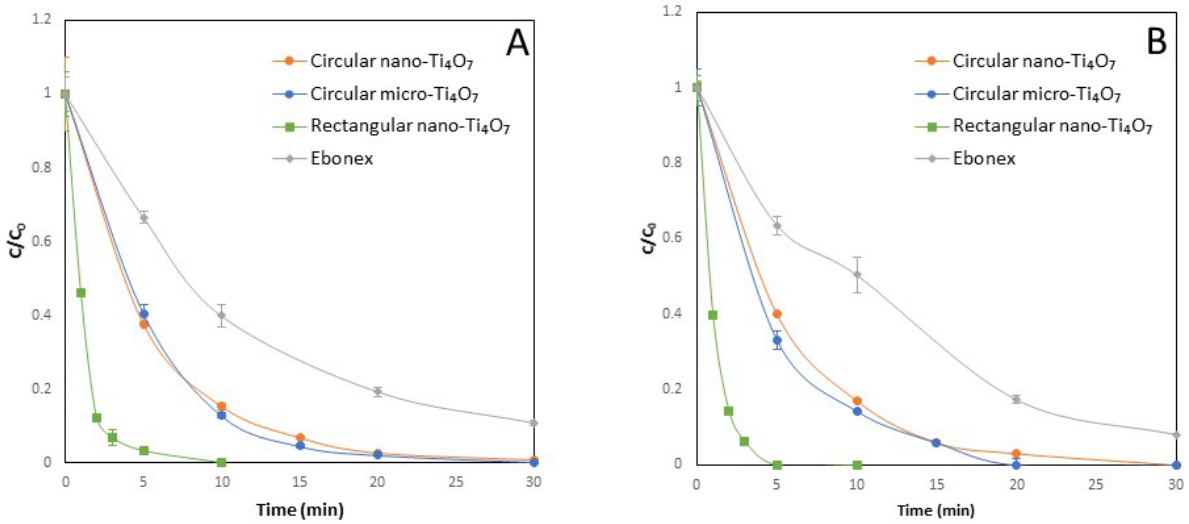

Figure 6. The concentration of L-PFOS (A) and B-PFOS (B) during EO treatment of PFOS in batch systems at 40 mA/cm^2 on circular nano-Ti_4O_7 (Reactor setup I), circular micro-Ti_4O_7 (Reactor setup I), rectangular nano-Ti_4O_7 (Reactor setup III) and Ebonex (Reactor IV). Initial PFOS concentration was at 2.0 μM. Error bar represents standard deviation (n=3).

The data presented in Figure 6 showed PFOS degradation under one current density, while a number of different current densities have been tested for each anode to enable a systematic comparison. For circular nano-Ti_4O_7 and circular micro-Ti_4O_7 anodes, thirteen different current densities from 2.5 mA/cm^2 to 210.0 mA/cm^2 were examined; for rectangular nano-Ti_4O_7, four different current densities from 5.0 mA/cm^2 to 40.0 mA/cm^2 were tested; while for Ebonex electrode, fourteen different current densities from 0.5 mA/cm^2 to 110.0 mA/cm^2 were examined. Higher current density would result in higher anodic potential, and the anodic potential corresponding to each current density was measured, which ranged from 1.0 V to 5.2 V vs. SSCE. The anodic potential is related to the generation of hydroxyl radical ·OH on the anode surface, which is the key oxidative agent causing PFAS degradation (Lin et al. 2018). Therefore, the k_{SA} is plotted against anodic potential in Figure 7 for all anodes for a comprehensive comparison of the anode materials and the anodic potentials. The k_{SA} of PFOS degradation on different anodes in batch mode are also listed in Appendix 3 Number #1-44 and 49.

As indicated in Figure 7, the k_{SA} of PFOS degradation increased along with the anodic potential in general. When anodic potential reached around 4.5 V, k_{SA} appeared to be plateaued for the circular nano-Ti_4O_7 and Ebonex anodes, indicating that the reaction rate became limited by mass transfer. The mass-transfer limited rate constant for the circular nano-Ti_4O_7 anode (1.30×10^{-3} m/s) was about ten folds of that for the Ebonex anode (1.27×10^{-4} m/s). However, for circular micro-Ti_4O_7 anode the k_{SA} stabilized between the anodic potential 3.5 to 4.5 V, and then increased again along with the anodic potential. This interesting pattern may be related to the dual modes of the pore size distribution of this anode shown in Figure 3, to which different mass transfer rates may apply. Although the data of rectangular nano-Ti_4O_7 are limited, it had the highest k_{SA} among the four anodes when the anodic potential ranged from 2.5 V to 3.0 V. Overall, all three Ti_4O_7 anodes have much greater reactivity than the Ebonex anode which is primarily Ti_9O_{17}. The three Ti_4O_7 anodes has different pore structures and distributions as shown in Figure 3, which might have impacted their reactivity by not only influencing the PFOS mass transfer but also modulating the surface electric potential distributions.

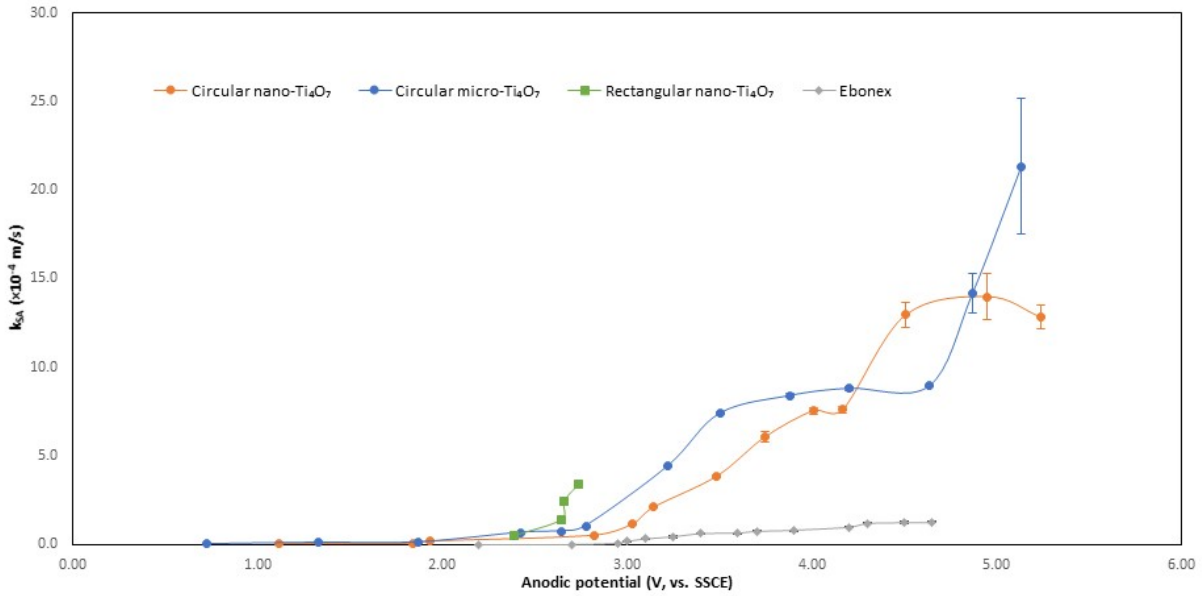

Figure 7. Surface area normalized rate constant in relation to the anodic potential (vs. SSCE) for L-PFOS degradation using circular nano-Ti_4O_7, circular micro-Ti_4O_7, rectangular nano-Ti_4O_7 and Ebonex anodes. Error bar represents standard deviation.

In addition to the four anodes described above, we have also prepared a circular micro-Ti_4O_7 electrode with graphene coated. It was prepared by a chemical vapor deposition method, in which a pre-made circular micro-Ti_4O_7 electrode was heated to 1150 ℃ under CH_4/Ar (1:10) atmosphere for 5 min (Li et al. 2013). This anode has been used for PFOS degradation in batch reactor at 20 mA/cm^2 and compared with those of the circular micro-Ti_4O_7 anode in Figure 8. The k_{SA} of L-PFOS degradation on circular micro-Ti_4O_7 and graphene-coated circular micro-Ti_4O_7 anodes were 1.11×10^{-4} m/s and 1.12×10^{-4} m/s. Graphene coating did not enhance the reactivity significantly. Therefore, graphene-coated anodes were not evaluated in other experiments in this study.

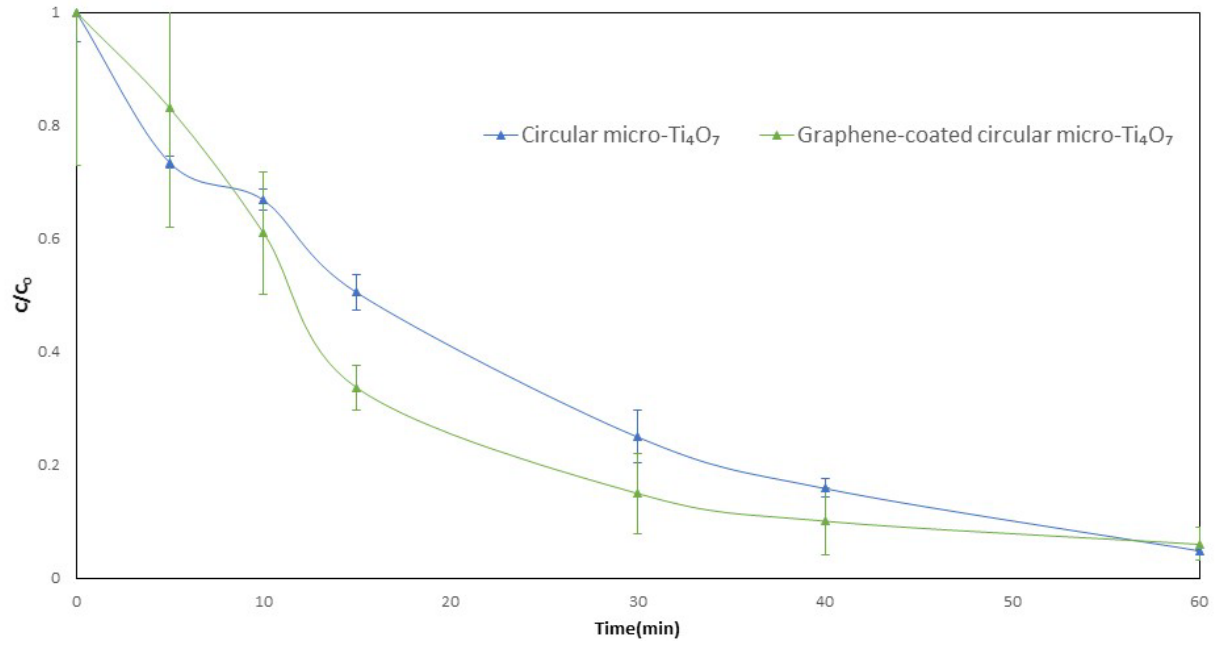

Figure 8. L-PFOS concentration during REM testament in Reactor I with circular micro-Ti_4O_7 and graphene-coated circular micro-Ti_4O_7 anode, respectively, at 20 mA/cm^2. Error bar represents standard deviation (n=3).

3.2.2 Energy consumption of PFOS degradation on different anodes

EE/O is defined as the electrical energy required to reduce the concentration of a pollutant by one order of magnitude (kWh/m^3) (Yang et al. 2018). It is a indicator of energy efficiency, and can be calculated by equation 3 below (Yang et al. 2018):

$$EE/O = \frac{U_{cell} I}{V} t_{90\%} \qquad (3)$$

where U_{cell} is the average cell voltage during EO treatment (V), I the applied current (A), $t_{90\%}$ the time for 90% PFOS removal (h), V the volume of reaction solution (L). The relationship between EE/O and current density exhibited a concave shape (Figure 9). The energy consumption for PFOS degradation on Ebonex was the highest among all anode materials, and EE/O reached the lowest (7.30 kWh/m^3) at the current density 4 mA/cm^2 on Ebonex anode. On circular nano-Ti_4O_7, circular micro-Ti_4O_7 anode and rectangular nano-Ti_4O_7 anode, the lowest value of EEO\/O were 3.45, 3.88 and 3.26 kWh/m^3 at the current density 20 mA/cm^2, 40 mA/cm^2 and 10 mA/cm^2, respectively. The anodic potentials for the lowest EE/O fell in the range of 2.6-3.2 V vs. SSCE for all four anode materials.

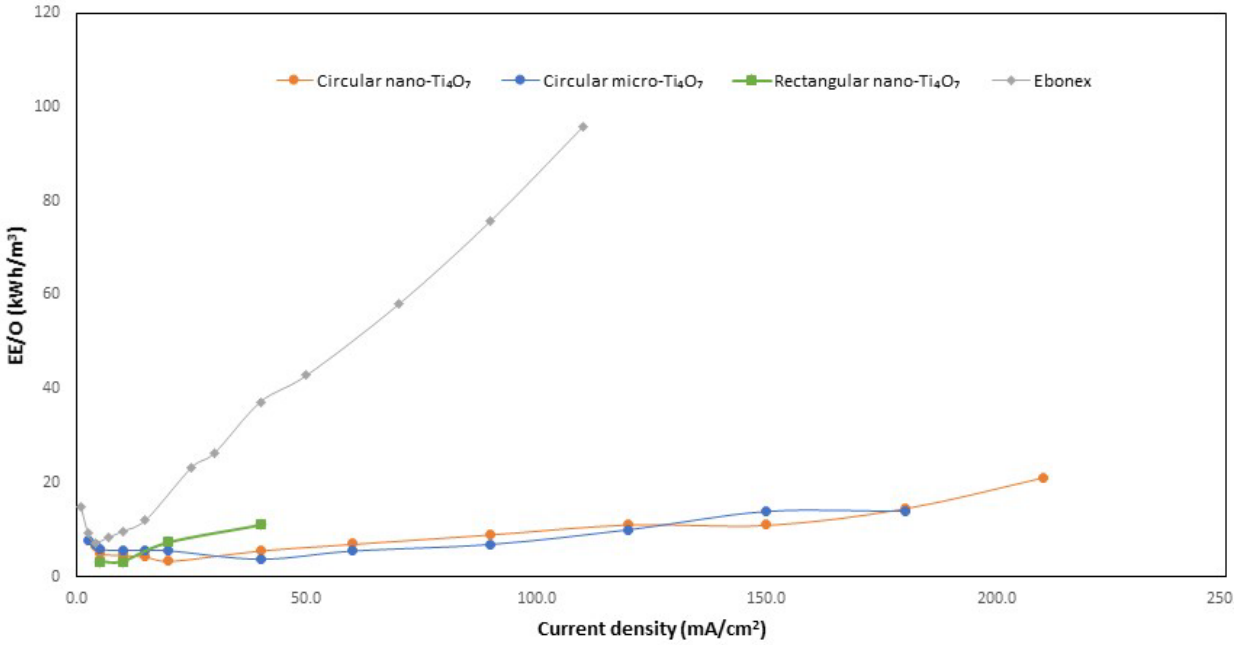

Figure 9. EE/O in relation to the current density for PFOS degradation during EO treatment in batch mode using different anode materials.

3.2.3 Impact of electrolyte and pH

In order to assess the influence of different electrolytes on EO efficiency, a set of experiments were performed in batch reactor II with rectangular nano-Ti_4O_7 anode in solutions with different supporting electrolytes under the current density of 10.0 mA/cm^2, including 10-mM, 25-mM and 100-mM Na_2SO_4, 100-mM $NaNO_3$ and 100-mM $NaClO_4$. The k_{SA} of L-PFOS degradation obtained in different electrolytes were summarized in Table 2, and also listed in Appendix 3 Number #45-49.

The k_{SA} for Na_2SO_4 solution decreased slightly with increasing electrolyte concentration, probably because the anodic potential was higher in the solution having lower concentration of electrolyte under the same current density. The k_{SA} did not vary much for the three electrolyte solutions at 100-mM.

Table 2. k_{SA} of L-PFOS degradation at 10.0 mA/cm^2 in solutions with different electrolytes

Electrolyte	k_{SA} (m/s)
10-mM Na_2SO_4	7.80×10^{-5}
25-mM Na_2SO_4	7.55×10^{-5}
100-mM Na_2SO_4	5.36×10^{-5}
100-mM $NaNO_3$	5.55×10^{-5}
100-mM $NaClO_4$	5.94×10^{-5}

The impact of pH on PFOS degradation was also evaluated in batch reactor II with rectangular nano-Ti_4O_7 anode at the current density of 5.0 mA/cm^2 in solution of 50-mM H_2SO_4, 100-mM NaOH and 100-mM phosphate buffer, respectively. The k_{SA} of L-PFOS degradation obtained in these solutions are shown in Table 3, and also listed in Appendix 3 #50-52. It appears that pH did not impact PFOS degradation much, although the k_{SA} was slightly smaller in the acidic solution. The lack of impact by solution pH is probably because PFOS degradation occurred on the anode surface where the pH is controlled more by the anodic reactions rather than the bulk solution.

Table 3. k_{SA} for L-PFOS degradation at 5.0 mA/cm^2 in solutions of different pH

Electrolyte	pH	k_{SA} (m/s)
50-mM H_2SO_4	1.95-2.20	3.43×10^{-5}
100-mM NaOH	12.40-12.55	4.73×10^{-5}
100-mM Phosphate Buffer	7.03-7.29	4.74×10^{-5}

3.2.4 Impact of TCE

PFOS degradation was also tested in the presence of trichloroethylene (TCE) as a co-contaminant. The experiment was performed in batch reactor III with 100-mM Na_2SO_4 solution containing 2 μM PFOS and TCE at different concentrations under 5.0 mA/cm^2. Because TCE is a volatile compound, the rector was placed in a gas-tight container for experiment (Figure 10A), and the profiles of PFOS concentration during EO treatment are presented in Figure 10B. The k_{SA} thus obtained in the presence of TCE at different concentrations are presented in Appendix 3 #54-58. The influence of TCE on PFOS degradation appeared to be minimal, if any, with k_{SA} at 5.50×10^{-5} m/s in the presence of 50 ppm TCE, while that in the absence of TCE was 6.84×10^{-5} m/s. Also seen in Figure 10B, more than 95% L-PFOS was removed from the system in 30 min regardless of the initial concentration of TCE.

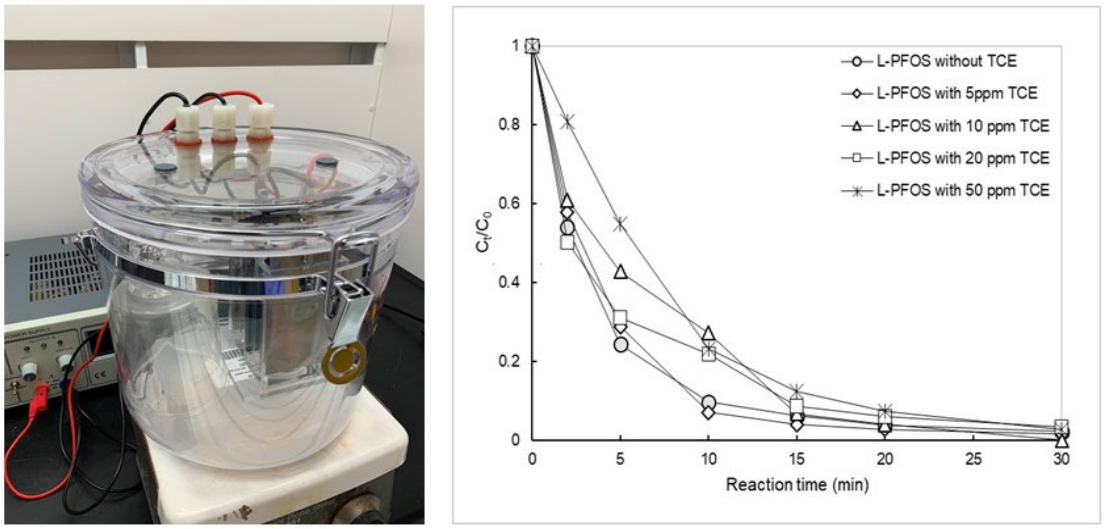

Figure 10. The gas tight container with batch reactor III enclosed for EO experiment (A). L-PFOS concentration during EO in 100-mM Na_2SO_4 solution in the presence of different concentration of TCE at 5.0 mA/cm^2 using rectangular nano-Ti_4O_7 anode (B).

3.3 Results: mixture of PFAAs

Experiments were conducted to evaluate the performance of selected batch systems on a mixture of PFAAs including PFBA, PFPeA, PFHxA, PFHpA, PFOA, PFBS, PFHxS and PFOS. The experiments were performed primarily in batch reactor III with the rectangular nano-Ti_4O_7 anode, and Ebonex anode was also tested for comparison.

3.3.1 Degradation of PFAAs on the rectangular micro-Ti_4O_7 anode

Figure 11 displays the concentration profile of each PFAA in the mixture solution during EO in batch mode using on rectangular nano-Ti_4O_7 anode at 15 mA/cm^2 current density as an example to show the behaviors. More than 90% of each PFAAs were removed after 8 hours, and especially L-PFOS and PFOA were completely removed within 30 min. The k_{SA} of each PFAA is listed in Apendix 4 #1-6 and 11-18, along with all other obtained from the experiments with PFAA mixture on the rectangular nano-Ti_4O_7 anode in batch mode under different current densities. The k_{SA} decreased in the order: L-PFOS > PFOA > L-PFHxS > PFHpA > PFHxA > L-PFBS > PFPeA > PFBA.

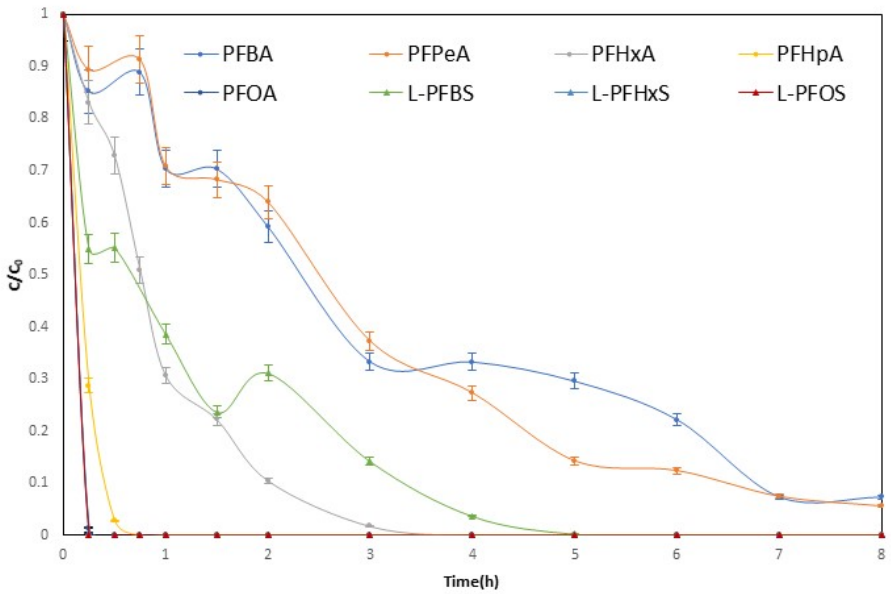

Figure 11. Concentration of each PFAA in the mixture solution of 100-mM Na_2SO_4 during EO in reactor III under 15 mA/cm^2 on rectangular nano-Ti_4O_7 anode. The initial concentration of each PFAA was 2.0 μM. Error bar represents standard deviation (n=3).

An experiment was also conducted to compare the degradation of PFAA with each spiked individually or in a mixture at the same initial concentration (2.0 μM) in reactor III with rectangular nano-Ti_4O_7 anode under the same current density 5.0 mA/cm^2. The obtained k_{SA} values are compared in Table 4. It appears that the k_{SA} in solution with PFAA spiked individually was not significantly different from that in a mixture, suggesting the absence of competition effect between PFAAs at the tested concentrations.

Table 4. The k_{SA} of PFAA obtained in experiment with it spiked individually or in mixture

Compound	Individual (m/s)	Mixture (m/s)
PFBA	2.17×10^{-7}	4.30×10^{-7}
PFPeA	3.66×10^{-7}	7.17×10^{-7}
PFHxA	1.80×10^{-6}	2.00×10^{-6}
PFHpA	7.50×10^{-6}	5.83×10^{-6}
PFOA	3.52×10^{-5}	2.45×10^{-5}
L-PFBS	1.05×10^{-8}	8.12×10^{-7}
L-PFHxS	1.05×10^{-5}	1.50×10^{-5}
L-PFOS	6.43×10^{-5}	6.67×10^{-5}

The degradation of PFAA was also evaluated in 100-mM Na_2SO_4 solution with all PFAAs spiked in mixture in batch reactor III with rectangular nano-Ti_4O_7 anode under different current densities. The obtained k_{SA} values are plotted in Figure 12 in relation to the chain lengths and the head functional groups. For each PFAA, the k_{SA} increased with increasing current density. For the PFAAs having the same functional group, the increase in carbon chain length led to greater reactivity. This is in accord with other studies showing shorter chained PFAA more recalcitrant to electrooxidation (Schaefer et al. 2015). For the PFAAs of the same carbon chain length, the one with sulfonate head group tend to degrade faster than that with carboxylic group.

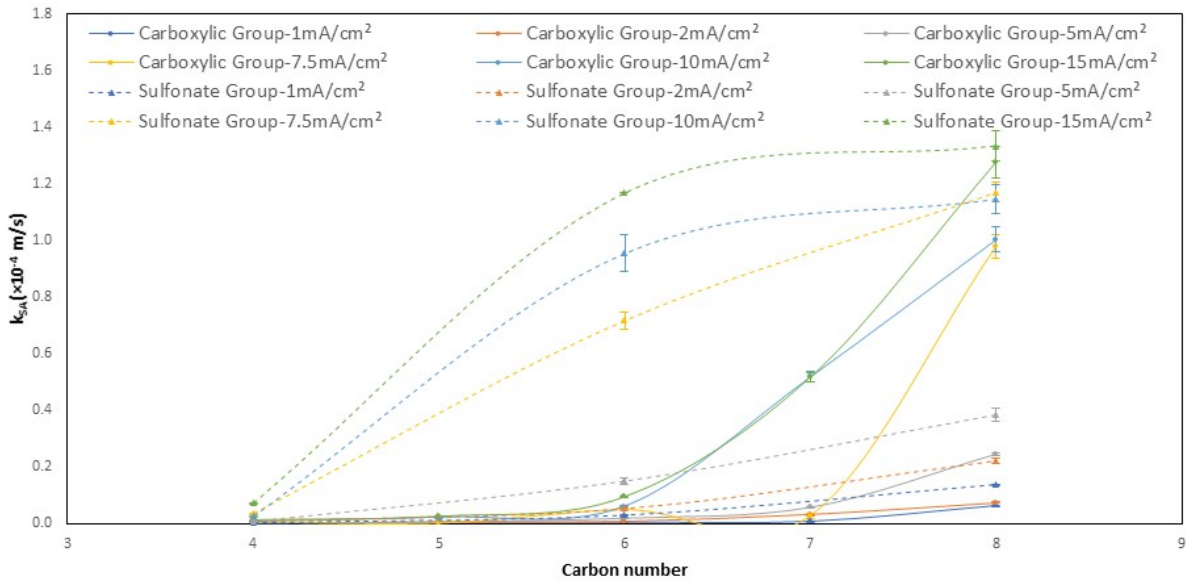

Figure 12. k_{SA} of PFAAs of different chain lengths and head functional groups, obtained in batch reactor III using rectangular nano-Ti_4O_7 anode in 100-mM Na_2SO_4 solution with all PFAAs spiked in mixture. Error bar represents standard deviation.

3.3.2 Degradation of PFAAs on Ebonex anode

The degradation of each PFAA in a mixture solution during EO in batch reactor IV with Ebonex anode at 15 mA/cm^2 is presented in Figure 13. More than 50% of each PFAA was removed at after 4 hours, while L-PFOS and PFOA were completely removed within 1 hour. The k_{SA} of each PFAA is listed in Appendix 4 #7-10, along with those obtained from the experiments with PFAA mixture on the Ebonex anode in batch mode under different current densities. The k_{SA} decreased in the order: L-PFOS > PFOA > L-PFHxS > PFHpA > PFHxA > L-PFBS > PFPeA > PFBA, an order essentially the same as those obtained on the rectangular nano-Ti_4O_7 anode discussed in 3.3.1.

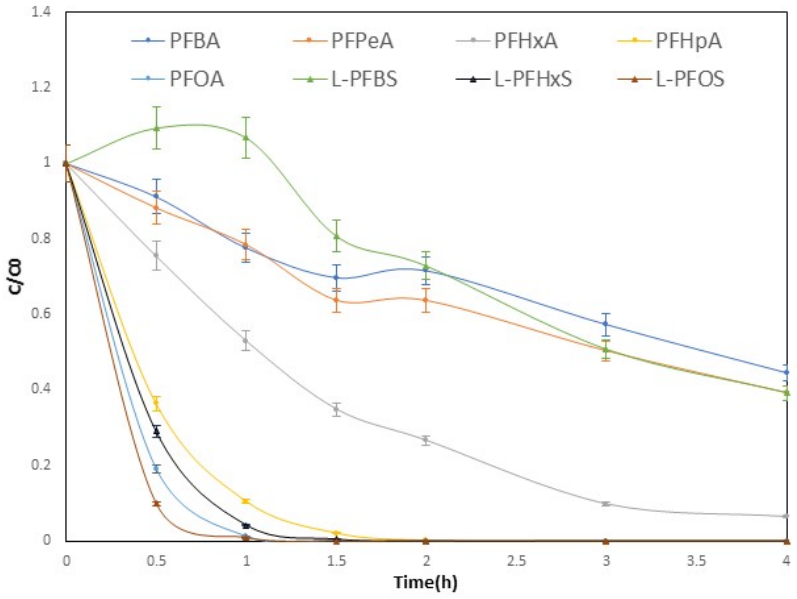

Figure 13. Concentration of each PFAA in the mixture solution of 100-mM Na_2SO_4 during EO in Reactor IV (100-mL solution) under 15 mA/cm^2 on Ebonex anode. The initial concentration of each PFAA was 2.0 μM. Error bar represents standard deviation.

The degradation of PFAA was also evaluated in 100-mM Na_2SO_4 solution with all PFAAs spiked in mixture in batch reactor IV with Ebonex anode under different current densities. The obtained k_{SA} values are plotted in Figure 14 in relation to the chain lengths and the head functional groups. The same pattern as that for the rectangular nano-Ti_4O_7 anode shown in Figure 12 was observed. For each PFAA, the k_{SA} increased with increasing current density. For the PFAAs having the same functional group, the increase in carbon chain length led to greater reactivity. This is in accord with other studies showing shorter chained PFAAs more recalcitrant to electrooxidation (Schaefer et al. 2015). For the PFAAs of the same carbon chain length, the one with sulfonate head group tend to degrade faster than that with carboxylic group.

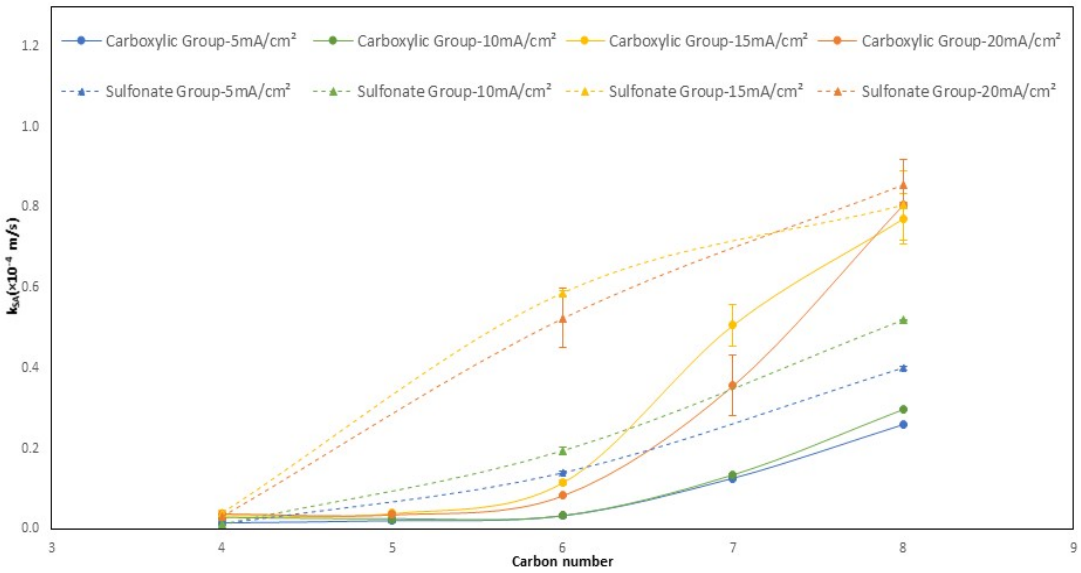

Figure 14. k_{SA} of PFAAs of different chain lengths and head functional groups, obtained in batch reactor IV (100-mL) using rectangular nano-Ti_4O_7 anode in 100-mM Na_2SO_4 solution with all PFAAs spiked in mixture. Error bar represents standard deviation.

Increased PFAA removed under higher current densities are ascribed to the higher anodic potentials as the current density increases. The k_{SA} is plotted against anodic potential in Figure 15 for both the Ebonex and rectangular nano-Ti_4O_7 anode. As seen in Figure 15, each PFAA was degraded at lower anodic potentials on the rectangular nano-Ti_4O_7 anode than on the Ebonex anode, and the k_{SA} tended to be greater, which was the same trend observed for PFOS when spiked individually in the solution (Figure 7). This indicates the better performance of the rectangular nano-Ti_4O_7 anode than the Ebonex anode for PFAA degradation.

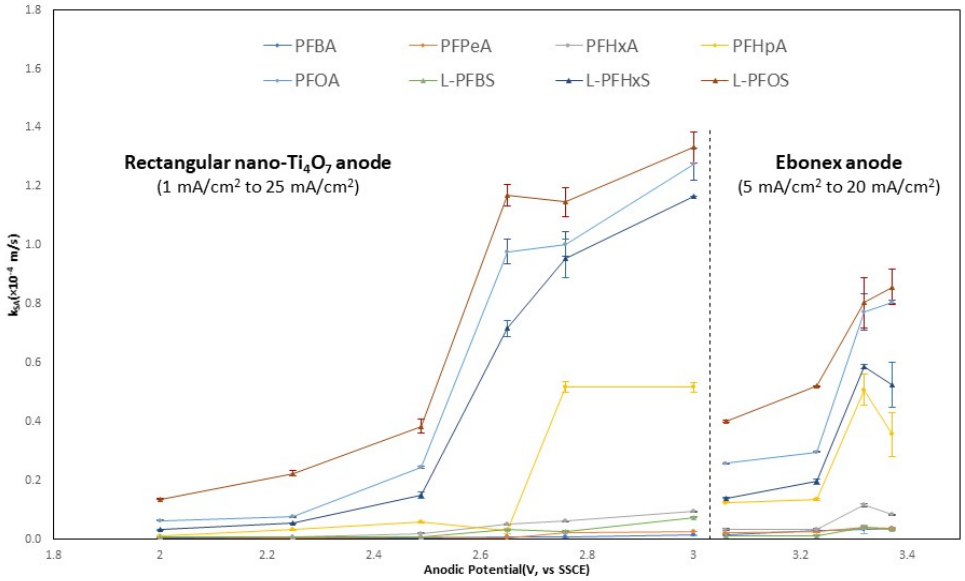

Figure 15. Surface area normalized rate constant in relation to the anodic potential (vs. SSCE) for PFAA in the mixture solution by EO in batch mode with rectangular nano-Ti_4O_7 and Ebonex anode. Error bar represents standard deviation.

3.4 Formation of fluoride during EO treatment of PFAAs

The formation of fluoride was measured in selected EO treatment systems as means to assess PFAA mineralization. Two methods have been employed for F- quantification as described in Section 3.1.2, one with ion chromatography (IC) and the other with fluoride ion selective electrode (ISE). Based on the fluoride concentration, a defluorination ratio (dF) was calculated by dividing the released F^- concentration by the total fluorine in the PFAA that has been removed from the system as shown in equation 4:

$$dF = \frac{[F^-]_t}{\sum n([PFAA]_0 - [PFAA]_t)} \times 100\% \qquad (4)$$

Where $[F^-]_t$ is the fluoride concentration at time t, $[PFAA]_0$ and $[PFAA]_t$ are PFAA concentrations at time 0 and t, respectively, and n is the number of fluorine contained in the PFAA.

In one experiment, a solution of 2.0-μM PFOS in 100-mM Na_2SO_4 was treated in Reactor III under 10 mA/cm^2 for 20 hours. The samples taken at the end of the treatment was analyzed by IC for F^- and by UPLC-MS/MS for PFOS concentration. PFOS was nearly completely removed while 39.47 μM fluoride was formed in the product solution. The defluorination ratio was thus calculated to be 115.38%.

Another experiment was also carried out in Reactor III with the mixture of PFAAs (each at 2.0 μM) in 100-mM Na_2SO_4 solution. EO treatment was performed at different current densities for 8 hours. The samples were collected at the end of the experiment and analyzed for concentrations of PFAAs and F^- by IC. The defluorination ratios were 20.07%, 79.45%, 117.32%, 71.69% and 72.27% when the current density was 2.0, 5.0, 7.5, 10.0 and 15.0 mA/cm^2. The IC method was validated by standard addition assessment, in which the recovery of the sample with 52.63 μM (1 ppm) F^- standard addition was 95.38%.

Experiments were also performed with F^- quantified by ISE method, in which a higher PFOS concentration was used because the sensitivity of ISE method is not as high as IC. A solution of 20.0 μM PFOS in 100-mM Na_2SO_4 was treated in Reactor IV with the Ebonex anode under 10 mA/cm^2 for 2.5 hours. Samples were taken at different time intervals, analyzed for PFOS and F^- concentration (by ISE). PFOS degradation increased over time along with more F^- release, with more than 99% PFOS removed after 2.5 h and 24.32 μM F^- released. The defluorination ratio was calculated to be 71.50% at 2.5 h (Figure 16). The ISE method was validated by standard addition assessment, in which the recovery of the sample with 5 ppm F^- standard addition was 118%.

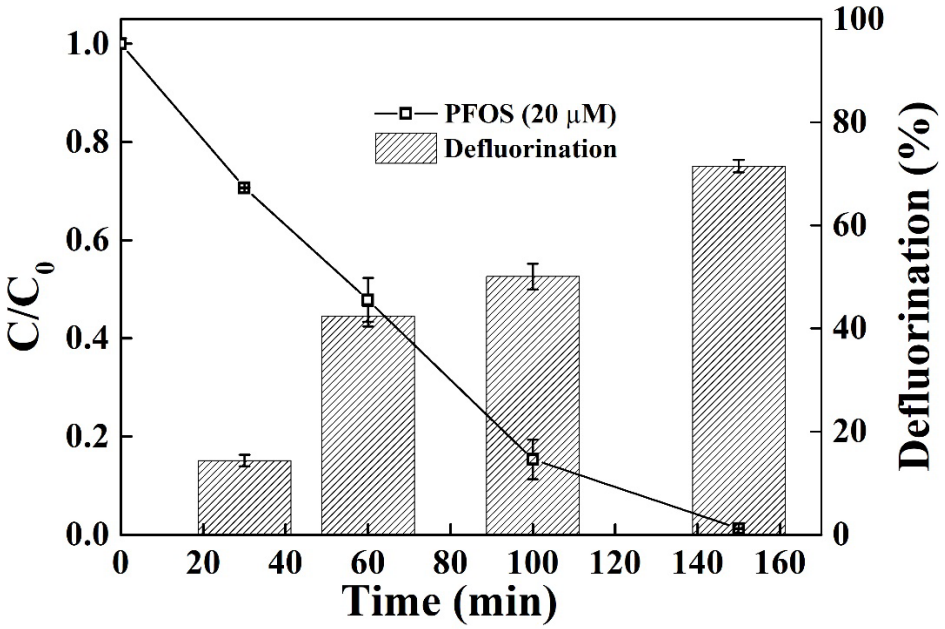

Figure 16. The change of PFOS concentration and defluorination ratio during EO treatment of 20 μM PFOS in 100-mM Na_2SO_4 solution in Reactor IV on Ebonex anode at 10 mA/cm^2. Error bar represents standard deviation (n=3).

3.5 Formation of chlorate and perchlorate

Chloride (Cl^-), a common anion in natural water, can form undesirable chlorate (ClO^{3-}) and perchlorate (ClO^{4-}) during EO treatment (Barazesh et al. 2016, Park et al. 2009). The transformation of Cl^- on boron doped diamond (BDD) anode is relatively well documented (Azizi et al. 2011, Lin et al. 2016). In this study, we evaluated the formation of chlorate and perchlorate during PFOS degradation on rectangular nano-Ti_4O_7 in the presence of Cl^- and compared it with that on the BDD. The experiments were carried out in Reactor III in 100-mM Na_2SO_4 containing 2-μM PFOS and 1-mM Cl^-, and the BDD anode has the same size with the rectangular nano-Ti_4O_7. The results of this experiment are presented in Figure 17.

As shown in Figure 17, the formation of chlorate and perchlorate was more rapid on BDD anode, with ClO^{3-} reaching temporal maximum of 427.8 μM in the first 0.5 h and then decreasing, while ClO^{4-} concentration increased and reached approximately 1 mM in 3.0 h. Formation of ClO^{3-} on the Ti_4O_7 anode was much slower, reached temporary maximum of approximate 382.0 μM in 4.0 h, and then decreased slowly. The formation of ClO^{4-} also appeared much slower on Ti_4O_7 anode and took 25.0 h to reach 0.95 mM. Note that the rates of chlorate and perchlorate formation was

much slower than PFOS degradation in this system which is completely removed within 0.5 h. The slow formation of ClO^{3-} and ClO^{4-} on the Ti_4O_7 anode indicates its less reactivity towards Cl^-, because the oxidation of Cl^- due to direct electron transfer (DET) on this anode did not occur, as opposed to that on BDD, as indicated by linear scan voltammetry (not shown). The slow rates of chlorate and perchlorate formation on Ti_4O_7 anode is an advantage for application of this type of anodes in water treatment.

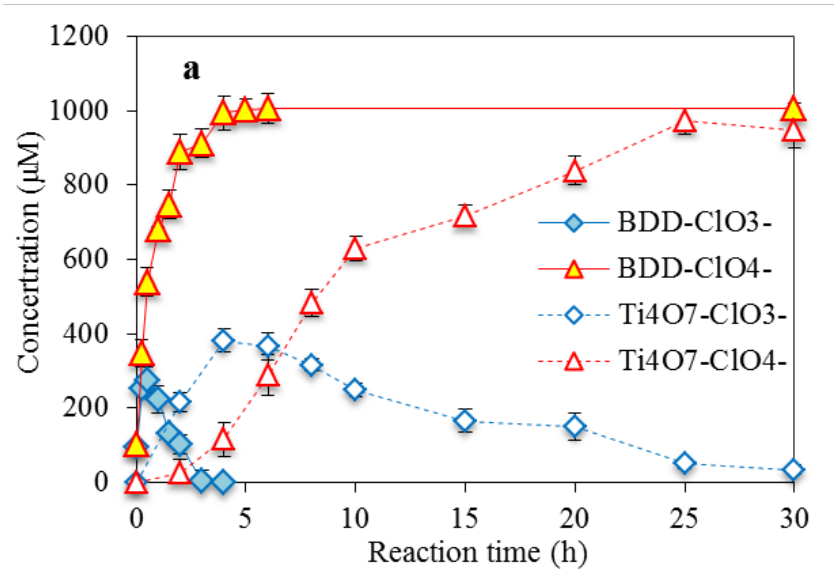

Figure 17. Formation of ClO^{3-} and ClO^{4-} during the electrooxidation of a solution containing 2.0-μM PFOS and 1-mM Cl^- on BDD and rectangular nano-Ti_4O_7 anode in Reactor III at the current density of 10 mA/cm^2.

3.6 Summary

We have evaluated four different TSO anodes, circular nano-Ti_4O_7, circular micro-Ti_4O_7, rectangular nano-Ti_4O_7 and Ebonex, in a series of batch EO treatment experiments in solutions with only PFOS spiked under different operation conditions in an attempt to compare the treatment efficiency of different anodes and the effects of major operation parameters. Effective PFOS degradation was observed with all anodes, with near stoichiometric formation of F^- in the systems for which fluoride had been tested. The three Ti_4O_7 anodes appeared to exhibit much greater performance than that of the Ebonex that is primarily composed of Ti_9O_{17}, according to their k_{SA} values in relation to anodic potential. These are also reflected by their energy consumption per log reduction of PFOS (EE/O) which was much higher for the Ebonex anode than the other three anodes. The three Ti_4O_7 anodes also exhibited some difference in terms of EO reactivity towards PFOS. These may be related to the difference in pore structures among the three anodes that can in turn impact mass transfer and electric potential distribution on the anode surface.

The change in electrolyte type, concentration and pH of the reaction solution appeared to have minimal if any impact on PFOS degradation by EO on TSO anodes. This is probably because the bulk solution conditions may have very little effect on the anode surface conditions that are controlled by the water oxidation reactions on the anode at our experiment conditions. The presence of TCE in the reaction solution also had very limited impact on the PFOS degradation during EO.

Experiments were also conducted to evaluate the performance of two anodes, rectangular nano-Ti_4O_7 and Ebonex, in batch systems on a solution of mixture PFAAs, including PFBA, PFPeA, PFHxA, PFHpA, PFOA, PFBS, PFHxS and PFOS. Degradation of all PFAAs can be observed, with near stoichiometric formation of F^- in some systems. The k_{SA} for PFAA in the mixture was not much different from that obtained when each PFAA was spiked in the solution individually, indicating the absence of strong competitive effect among the PFAA in the mixture under the experiment conditions. Based on the pattern of k_{SA} values in relation to anodic potential for each PFAA, the Ti_4O_7 anode has greater performance than that of the Ebonex. For the PFAAs having the same head acid group (carboxyl vs. sulfonate), the increase in carbon chain length led to greater reactivity. For the PFAAs of the same carbon chain length, the one with sulfonate head group tend to degrade faster than that with carboxylic group.

Batch EO treatment experiments were also performed to evaluate the formation of chlorate and perchlorate during PFOS degradation on rectangular nano-Ti_4O_7 in the presence of Cl^- and compared with that on the BDD anode. It showed that the formation of chlorate and perchlorate was much slower on the Ti_4O_7 anode than on the BDD anode. This is because the oxidation of Cl^- due to direct electron transfer (DET) on Ti_4O_7 anode did not occur as opposed to BDD. The slow rates of chlorate and perchlorate formation on Ti_4O_7 anode is an advantage for application of this type of anodes in water treatment.

4 REM treatments

This section describes the experiments to evaluate the performance of reactive electrochemical membrane (REM) systems involving TSO anodes, along with the results and discussions. A REM system is a filtration device with an electric-conductive porous ceramic membrane that serves simultaneously as a three-dimensional (3-D) anode and a membrane through which contaminant-containing water is filtered and treated electrochemically. In this study, we have fabricated two REM systems that were respectively used for the tubular Ebonex anode and the circular nano-Ti_4O_7 anode. Experiments were performed with these REM systems first with solutions only having PFOS spiked for comparison of the anode materials and major operation conditions (Section 4.2). The REM systems were then evaluated on a mixture of PFAAs including PFBA, PFPeA, PFHxA, PFHpA, PFOA, PFBS, PFHxS and PFOS (Section 4.3). The formation of chlorate and perchlorate were also evaluated in selected systems (Section 4.4).

4.1 Experiments

4.1.1 Reactor setup

Two REM reactors were fabricated that were respectively used for the tubular Ebonex anode and the circular nano-Ti_4O_7 anode, as described below.

REM reactor for the tubular Ebonex anode: This REM reactor is composed of a hollow cylindrical vessel (110 mm length, 50 mm diameter) made by acrylic, having the tubular Ebonex anode housed coaxially in the middle (Figure 18A), and the actual reactor setup is shown in a picture in Figure 18B. A 316 stainless steel rod is placed in the middle of the tubular Ebonex REM as the cathode. A leak-free Ag/AgCl electrode worked as the reference electrode. A feed inlet and a retentate outlet are installed on either end of the vessel to allow sample solution flow through the tubular channel of the Ebonex anode, and an outlet installed on the side of the vessel to collect permeate filtrating through the anode.

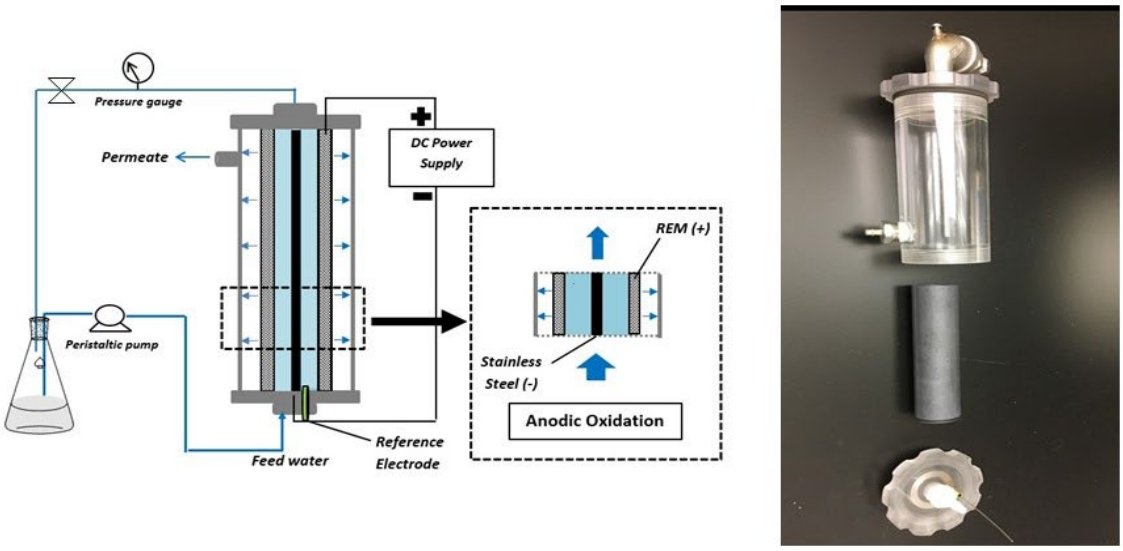

Figure 18. A schematic diagram of REM reactor with Ebonex anode in cross-flow filtration operation (A); a picture of actual reactor (B).

REM reactor for the circular nano-Ti_4O_7 anode: The reactor is also composed of an hollow cylindrical vessel (45 mm length, 60 mm diameter) made by acrylic, with the circular nano-Ti_4O_7 anode installed in cross-sectional direction, and a circular 316 stainless steel plate of the same size installed in parallel at 1.2 cm gap as the cathode (Figure 19A), and a picture of the actual reactor is shown in Figure 19B. A leak-free Ag/AgCl electrode worked as the reference electrode. A feed inlet and a retentate outlet are installed to allow sample solution flow through the space between the cathode and the anode, while another outlet was installed on one end to collect permeate filtrating through the anode.

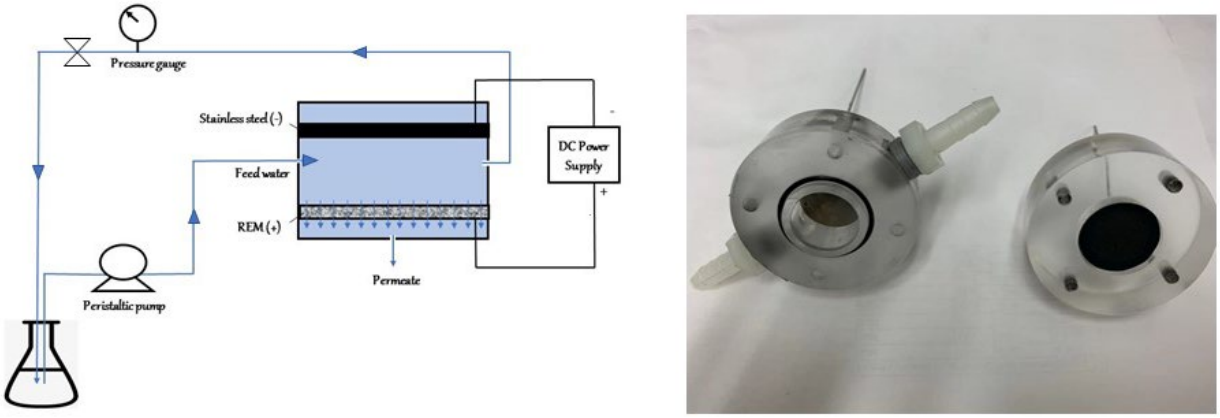

Figure 19. A schematic diagram of REM reactor with circular nano-Ti_4O_7 anode in cross-flow filtration operation (A); a picture of actual reactor (B).

REM operation: The REM was operated in a cross-flow filtration mode, in which the sample solution was fed to the reactor at a constant flow rate via MasterFlux L/S pump. The retentate flow was recycled to the feed tank while the permeate flow was not. The backpressure of the retentate outflow was adjusted to achieve a prescribed permeate flow rate filtered through the REM membrane. The system was first operated without electricity supplied till PFAA concentrations in permeate reach that in the feed solution. A 303 DM DC power supply (Electro Industries, USA) was then used to supply electricity at varying current densities to the REM device. The reaction solution contained 2.0-μM PFOS or a PFAA mixture having the same components as in the batch reactor study, each at 2.0 μM, with 25-mM or 100-mM Na_2SO_4 as supporting electrolyte. 400 μL samples were withdrawn from both the retentate and permeate for analyzing PFOS or PFAA concentrations at prescribed time intervals. PFAA concentration was analyzed using the same protocol describe in 3.1.2.

4.1.2 Reaction rate analysis

The data collected from the REM treatment in cross-flow filtration mode were used to calculate the pseudo-first order reaction rate constant (k) of PFAA by the following plug flow reactor model (Schmidt 2005):

$$k = -ln\frac{C_p}{C_f} \times \frac{u}{x} \qquad (5)$$

Where u is the linear flow velocity (m/s); x the thickness of REM (m), C_p the average substrate concentration (mol/L) in the permeate, C_f the substrate concentration (mol/L) in the feed solution.

4.2 Results: PFOS degradation

4.2.1 Tubular Ebonex REM

Experiments were performed with the tubular Ebonex REM to treat a solution containing 2.0 µM PFOS in 100 mM Na_2SO_4 in cross-flow filtration mode over a range of applied current densities (0.5 – 4.0 mA/cm^2), and the results are presented in Figure 20. The electric current was not applied for the first 40 min of the experiment, during which the L-PFOS concentration in the permeate did not differ from that in the feed (Figure 20A), indicating that adsorption of PFOS to the membrane electrodes was limited, if any. Once applied by electric current, the PFOS concentration in the permeate decreased immediately and maintained stable between the period 60-120 min when electricity was supplied. L-PFOS removal increased with the applied current density, reaching 97.4%-98.7% at 4.0 mA/cm^2. The pseudo-first order reaction rate constant (k) was calculated to be 0.0035 s^{-1}, 0.0093 s^{-1}, 0.0104 s^{-1} and 0.0868 s^{-1} for 0.5, 1.0, 2.5 and 4.0 mA/cm^2 treatment, respectively. When the electric current was stopped at 120 min, the PFOS concentration in the permeate increased back to that in the feed, indicating that the removal of PFOS in permeate stream was attributed to electrochemical degradation. The concentration of L-PFOS in the retentate remained stable throughout the experiment. B-PFOS exhibited very similar behavior as that of L-PFOS (Figure 20B). Therefore, only L-PFOS is included in subsequent discussion on REM, while the reaction rate constants (k) for both L-PFOS and B-PFOS are reported in Appendix 5. All k values obtained for PFOS degradation on Ebonex REM are presented in Appendix 5 #1-13.

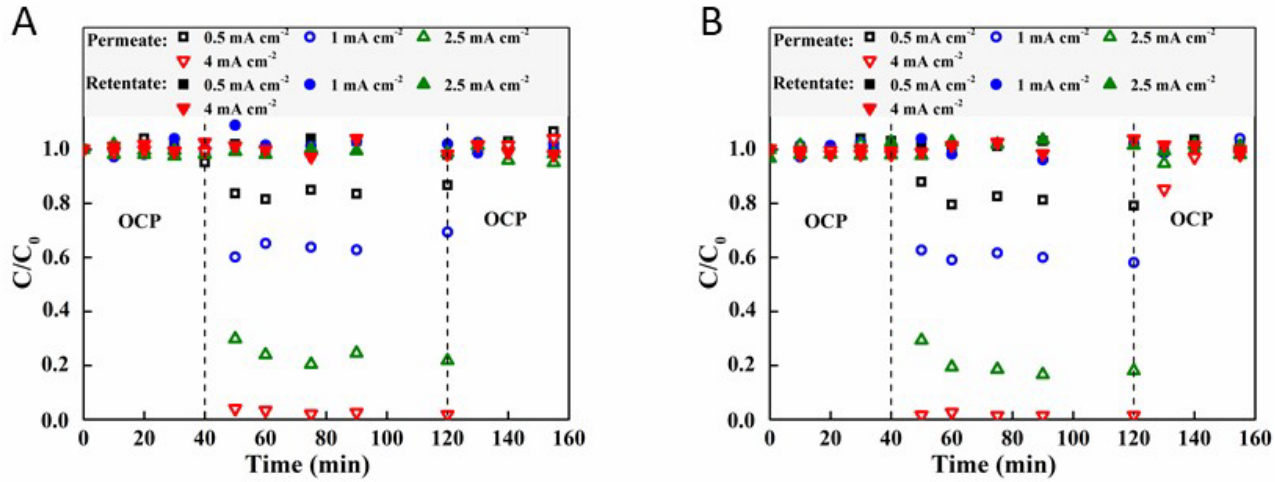

Figure 20. PFOS concentration in feed and permeate during treatment by the tubular Ebonex REM in cross-flow filtration mode at different current density (0.5 – 4.0 mA/cm^2); L-PFOS (A); B-PFOS (B). The permeate linear flow velocity was 0.079 cm/min.

An electric impedance analysis was performed on the tubular Ebonex anode in REM mode, and the active electrochemical surface area was measured to be 0.968 m^2. This can be sued to calculate the pseudo-first order rate constant normalized by the electrochemical surface area (k'_{SA}) by equation (6) (Zaky and Chaplin 2013).

$$k'_{SA} = k\frac{V}{S_{active}} \qquad (6)$$

Where k is the pseudo-first order reaction rate, S_{active} the electro-active surface area (m^2), V the treatment solution volume corresponding to the electro-active electrode surface area (m^3), which is the pore volume with the anode that was calculated from its porosity (17.29 %) in this case. The thus obtained k'_{SA} values are displayed in Figure 21 with regard to anodic potential. The active electrochemical surface area of the Ebonex anode was also measured by electric impedance analysis in batch mode (0.283 m^2), which can be used to calculate the k'_{SA} for the batch reactor treatment. The k'_{SA} obtained for the batch reactor treatment using Ebonex anode are also displayed in Figure 21 for comparison. It can be seen that the k'_{SA} for REM operation is significantly larger than that for the batch reactor. It is believed that REM enhanced the EO efficiency by promoting interphase mass transfer via convection facilitated dispersion (Zaky and Chaplin 2013).

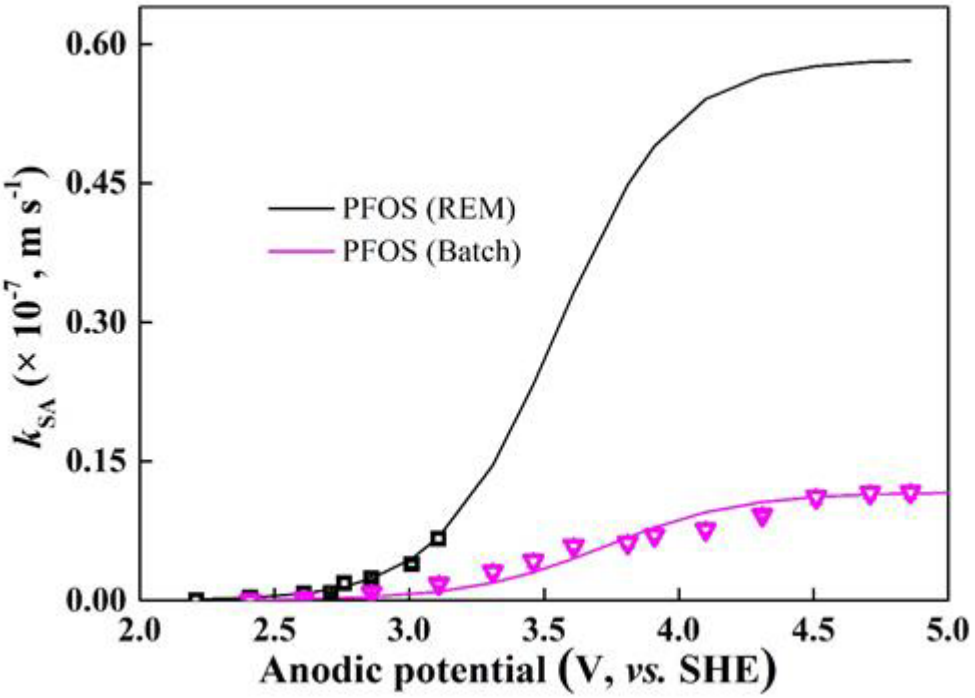

Figure 21. Pseudo-first order rate constant normalized by the electrochemical surface area (k'_{SA}) for PFOS oxidation on Ebonex anode in REM and batch mode. The solid line represent results modeled by interphase electrochemical reaction equation.

An experiment was also conducted to investigate the influence of filtration flow rate on the removal of PFOS, which was controlled by the retentate back pressure. As seen in Figure 22, PFOS removal increased with the decrease of back pressure. The decrease in backpressure led to lower permeate linear flow velocity and thus higher residence time of the sample solution in the REM membrane, which may have caused higher PFOS removal. The k value for the treatment at 1.24, 0.69, 0.49, 0.21 bar backpressure was respectively 0.0081 s^{-1}, 0.0093 s^{-1}, 0.0093 s^{-1} and 0.0064 s^{-1} relatively stable.

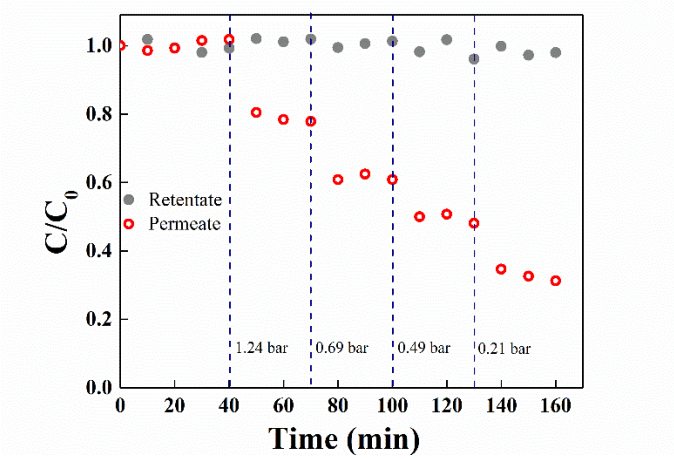

Figure 22. PFOS concentration in feed and permeate during treatment by the tubular Ebonex REM in cross-flow filtration mode at the current density of 1.0 mA/cm^2. The permeate linear flow velocity was 0.140, 0.079, 0.056, 0.024 for 1.24, 0.69, 0.49, 0.21 bar backpressure, respectively.

4.2.2 Circular nano-Ti_4O_7 REM

Experiments were performed with the circular nano-Ti_4O_7 REM to treat a solution containing 2.0 μM PFOS and 25 mM Na_2SO_4 in cross-flow filtration mode with applied current density of 10, 20 and 40 mA/cm^2. Electric current was not applied for the first 90 min of the REM operation, during which PFOS concentration in the permeate was reduced for the first 30 minutes and then approached to that in the feed solution (C_0) (Fig 23). This reflected a sorption and breakthrough behavior of PFOS in the porous nano-Ti_4O_7 medium. PFOS concentration in the permeate dropped immediately when the electric current was applied at 90 min and maintained at the low level during 90-210 min when the current was supplied. The reaction rate constant (k) was 0.049 s^{-1}, 0.169 s^{-1} and 0.196 s^{-1} for the current density 10 mA/cm^2, 20 mA/cm^2, and 40 mA/cm^2 respectively. All k values obtained for PFOS degradation on circular nano-Ti_4O_7 REM are presented in Appendix 5 Number 14-16.

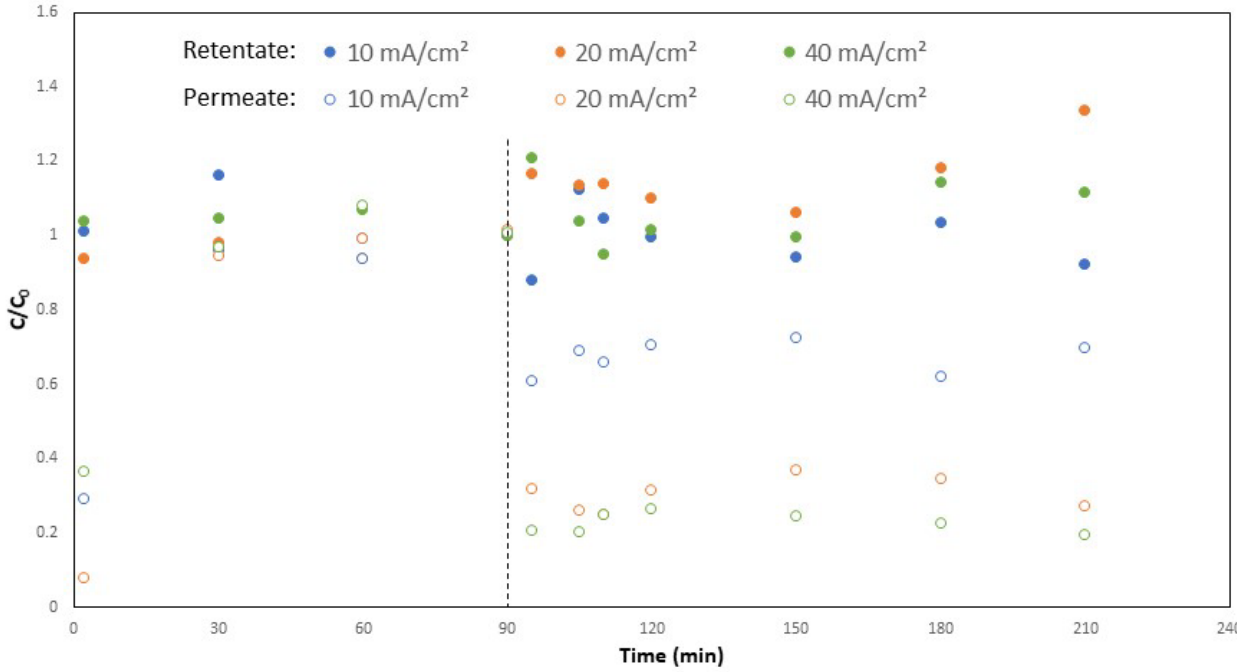

Figure 23. PFOS concentration in retentate and permeate during treatment by circular nano-Ti_4O_7 REM in cross-flow filtration mode at the current density of 10, 20 and 40 mA/cm^2. The permeate linear flow velocity was 0.02 cm/min.

The *k* values of PFOS degradation on the Ebonex REM and the circular nano-Ti_4O_7 REM are compared in Figure 24 with regard to anodic potentials. For similar anodic potential, the *k* of PFOS degradation was much greater on the circular nano-Ti_4O_7 REM than the tubular Ebonex REM, similar to that in the batch mode as shown in Figure 7. The *k* was calculated by equation 5, which is normalized to the thickness of the membrane (x), and where the linear flow velocity was calculated by dividing volumetric flow rate by flow pass cross-section area and porosity, therefore also normalized to the filtrate cross-section area. Hence, *k* can be used to compare reactivity across different REM reactor setups on a normalized basis.

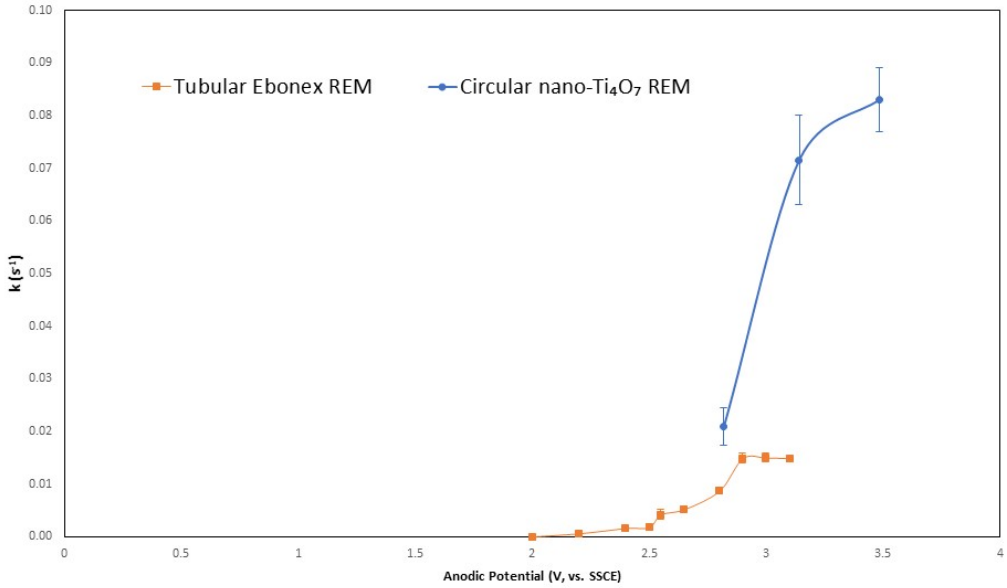

Figure 24. The relationship between *k* of L-PFOS degradation by REM treatment using different anodes with the anodic potential (vs. SSCE).

One interesting observation is that sorption of PFOS occurred on the circular nano-Ti_4O_7 material, but not on the Ebonex. PFOS appeared to adsorb on micro-Ti_4O_7 material even much stronger than that of the nano-Ti_4O_7 material. In one test, the REM with a circular micro-Ti4O7 anode was operated in cross-flow filtration mode without electric current applied for 30 h, and still there was no sign of PFOS breakthrough (Fig 25). For the first 3 h, the permeate flow was at 0.02 cm/min and was not recycled, while the PFOS concentration in the permeate flow remained at near zero and that in the retentate was close to the feed solution. From 3 h to 18 h, the permeate was recycled to feed tank with linear velocity remaining 0.02 cm/min, during which the PFOS concentration in the permeate remained at near zero and that in the retentate decreased over time, indicating a strong sorption of PFOS on the micro-Ti_4O_7 medium. From 18 h to 14 h, the permeate linear velocity was increased to 1.10 cm/min, the feed solution was replaced with fresh 2.0-μM PFOS and the permeate was no longer recycled, during which the PFOS concentration in the permeate was still at zero and that in the retentate increased back to the feed solution. Therefore, EO treatment experiment was not performed on micro-Ti_4O_7 REM. Such sorption however did not occur in the batch experiments, for example, as indicated in Figure 5 for circular nano-Ti_4O_7 material.

The different sorption behaviors between batch and filtration operation and the drastic difference in PFOS sorption capacity of the TSO materials in filtration process may relate to their porous structures shown in Figure 3. The micro-Ti_4O_7 material has a significant fraction of nanopores while that is minimal in the nano-Ti_4O_7 material and absent in the Ebonex. The nanopores may facilitate micro-bubble formation when water containing the surface-active compound, PFOS, passing through the medium as indicated in an earlier study (Yu et al. 2009). Such sorption behavior was however not effective in a batch reactor operation, where the nanopores inside the medium was not available without PFOS solution filtered through. Such sorption behavior during PFAA filtering through a porous medium seems also dependent on the solution ionic concentrations. We have attempted experiments with PFOS spiked in 100-mM Na_2SO_4 solution on the nano-Ti_4O_7 medium, but the PFOS sorption was found stronger and it took much longer

time to break through than that shown in Figure 23. The strong sorption of PFOS or other PFAAs on the Ti_4O_7 material may be one phenomenon that can be exploited in REM treatment where PFAAs can be first concentrated on the anode via sorption and then degraded by EO, which is worth of further study.

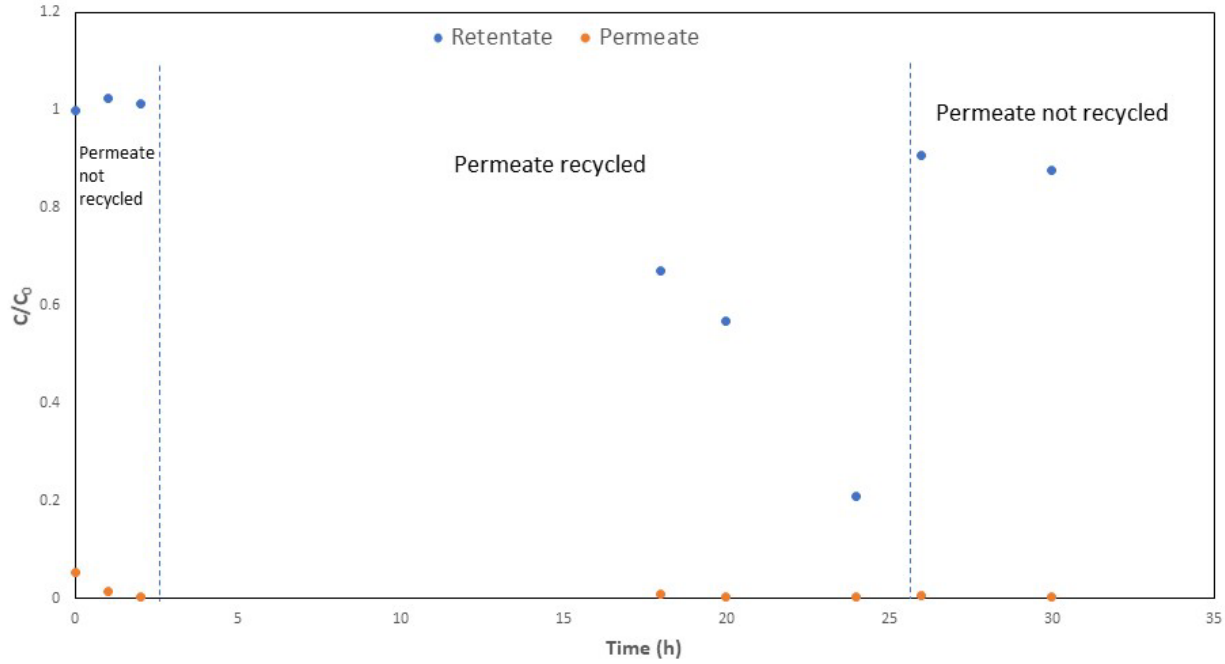

Figure 25. PFOS concentration in retentate and permeate during treatment by circular micro-Ti_4O_7 REM in cross-flow filtration mode with no current applied. The permeate linear flow velocity was 0.02 cm/min for the first 18 hours and 1.10 cm/min after 18 hours.

4.2.3 Energy consumption of PFOS degradation on different anodes

The electrical energy required to reduce the PFOS concentration by one order of magnitude (EE/O) can also be calculated for REM treatment. To this end, the linear velocity needed to achieve 90% PFOS reduction ($\mu_{90\%}$) can first be calculated from equation (5) by assuming $C_p/C_f = 0.1$, and then based on $V = \mu_{90\%}\rho St$, where ρ is porosity and S is the cross-sectional area of the flow pass. Equation (7) can be rearranged as:

$$EE/O = \frac{U_{cell} I}{\mu_{90\%}\rho S} \qquad (7)$$

The EE/O for PFOS degradation by REM with the tubular Ebonex anode are shown in Figure 26 with regard to anodic potential, and those obtained in batch reactor using the same anode are also displayed in Figure 26 for comparison. For both REM and batch reactors, EE/O exhibited a similar trend with regard to anodic potential, decreasing to a minimum point and then increasing. The minimum EE/O for REM was 1.37 kWh/m^3 at 2.9 V vs. SSCE, while that for batch reactor was 7.30 kWh/m^3 at 3.0 V vs. SSCE. The EE/O for REM was much lower than that of batch reactor, indictive of the enhanced efficiency of REM. REM enhances EO efficiency not only by increasing substrate interphase mass transfer rates via convection facilitated dispersion but also making more anode surface available for reaction with the solution filtered through the REM.

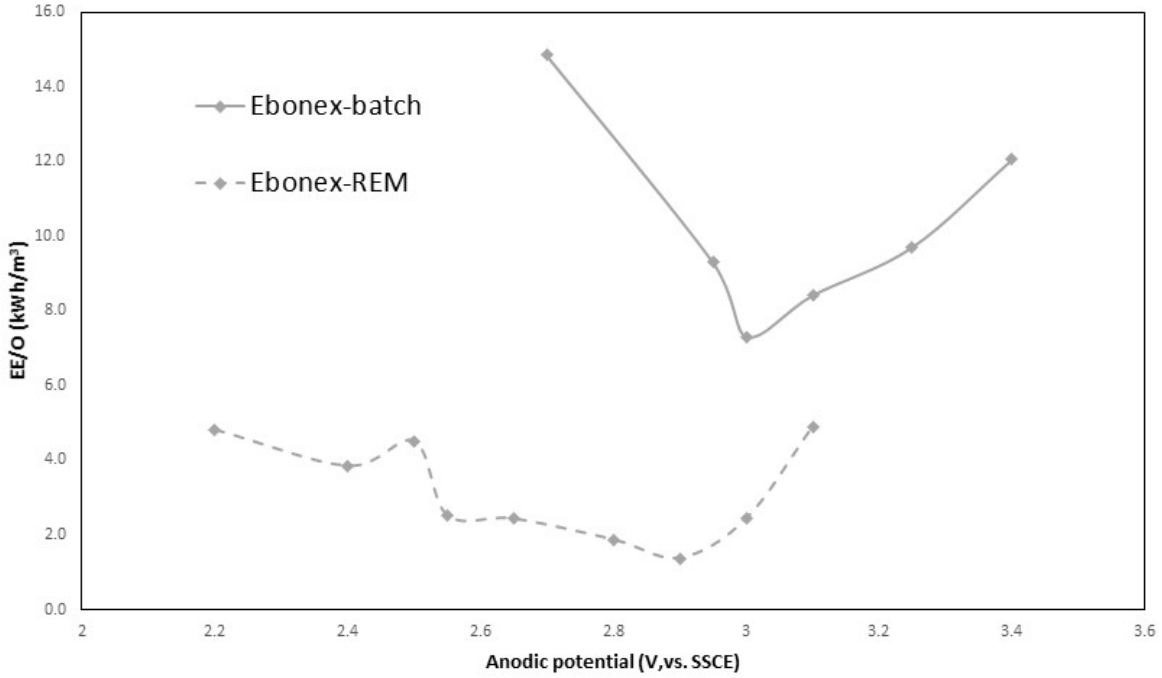

Figure 26. EE/O in relation to the anodic potential for PFOS degradation in 100-mM Na_2SO_4 solution during EO treatment in REM or batch reactor.

4.3 Results: PFAA mixture

4.3.1 Tubular Ebonex REM

An experiment was conducted to evaluate the performance of tubular Ebonex REM on a mixture of PFAAs including PFBA, PFPeA, PFHxA, PFHpA, PFOA, PFBS, PFHxS and PFOS. Long-chain PFAAs were removed more effectively than the shorter chain ones (Figure 27). An accumulation of PFBA was observed with its C/C_0 gradually rose over 1. This may indicate the formation of PFBA as a result of long-chain PFAA degradation. Formation of PFBA as an intermediate product of PFOS degradation was also observed in the batch reactor study, but only at trace level in the early treatment time (< 10 min) and disappeared at longer EO time. The more evident accumulation of PFBA in the REM treatment may be because of the short residence time associated with the REM treatment (5 mins at the 0.079 cm/min permeate linear velocity used in this experiment). The pseudo-first order reaction rate constant *k* of each PFAA degradation on the Ebonex REM has been calculated and presented in Appendix 6 Number #3. The *k* decreases in the order: PFHxA>PFOA>L-PFOS>PFHpA>L-PFHxS>PFPeA>L-PFBS>PFBA. This order is slightly different from that obtained in a batch reactor (L-PFOS > PFOA > L-PFHxS > PFHpA > PFHxA > L-PFBS > PFPeA > PFBA). In general, it appears that the degradation of PFCAs become faster than that of PFSAs in REM.

The k'_{SA} values of each PFAA degradation by tubular Ebonex REM were calculated and compared to that of the batch system in Table 5. It can be seen that for most PFAA the k_{SA} increased significantly.

Table 5. k_{SA} for each PFAA degradation at 5.0 mA/cm² in batch mode and cross flow mode.

Compound	$\mathbf{k'_{SA}}$ in batch mode (m/s)	$\mathbf{k'_{SA}}$ in cross flow mode(m/s)
PFBA	1.50×10^{-10}	-
PFPeA	2.01×10^{-10}	5.31×10^{-9}
PFHxA	3.23×10^{-10}	1.19×10^{-8}
PFHpA	1.24×10^{-9}	9.19×10^{-9}
PFOA	2.55×10^{-9}	1.06×10^{-8}
PFBS	1.25×10^{-10}	2.97×10^{-9}
PFHxS	1.38×10^{-9}	7.79×10^{-9}
PFOS	3.95×10^{-9}	1.05×10^{-8}

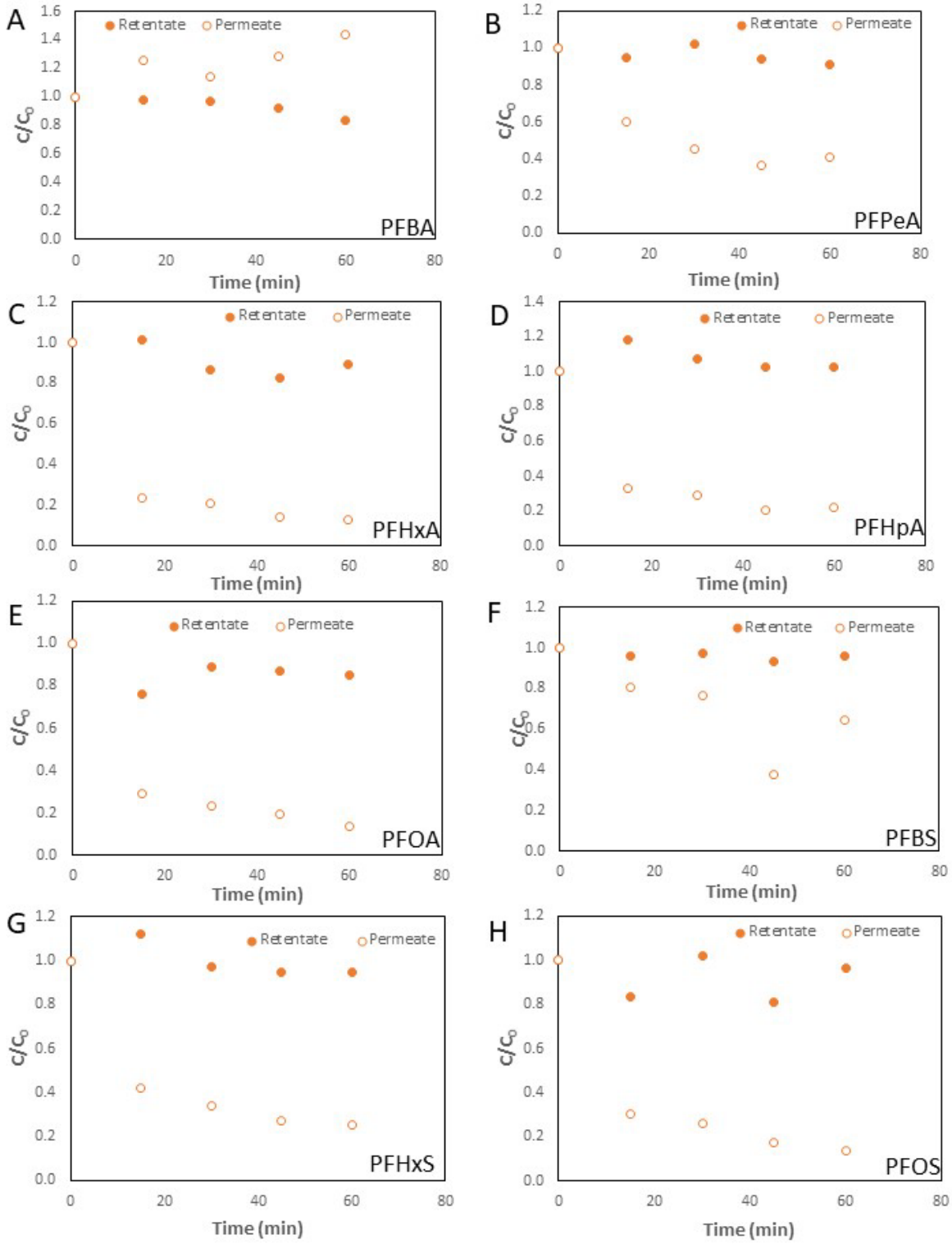

Figure 27. PFAA concentration in retentate and permeate during treatment of the PFAA mixture in 25-mM Na_2SO_4 by tubular Ebonex REM in cross-flow filtration mode at the current density of 5 mA/cm^2. The permeate linear flow velocity was 0.079 cm/min.

4.3.2 Circular Ti_4O_7 REM

Experiments were performed to evaluate the performance of nano-Ti_4O_7 REM on the mixture of PFAAs in 25-mM Na_2SO_4 solution under the current density of 20 and 40 mA/cm^2 (Figure 28). As that on the tubular Ebonex REM, the long-chain PFAAs were removed more effectively than the short chain ones. Over 80% of PFHpA and PFOA were removed through only one-time permeation, while the removal of PFPeA, PFHxA, PFHpA, PFOA and PFOS were degraded over 50%. The *k* of degradation of each PFAA on the nano-Ti_4O_7 REM has been calculated and presented in Appendix 6 Number #3. In general, the *k* was greater with the current density 40 mA/cm^2 than those of 20 mA/cm^2, and decreased in the order: PFOA>PFHpA>L-PFOS>PFHxA>PFPeA>L-PFHxS>L-PFBS>PFBA. The order differs from those obtained in the batch reactor with the same anode (L-PFOS > PFOA > L-PFHxS > PFHpA > PFHxA > L-PFBS > PFPeA > PFBA). Like that for the Ebonex anode, the degradation of PFCAs seems to become faster than that of PFSAs in REM than the batch reactor. The difference in the order of PFAA degradation *k* values for the REM and batch reactor treatments may be because the microporous structure within the TSO membranes that were made available during REM cross-flow filtration operation differs from that on the surface only of which was available for the batch reactor treatments.

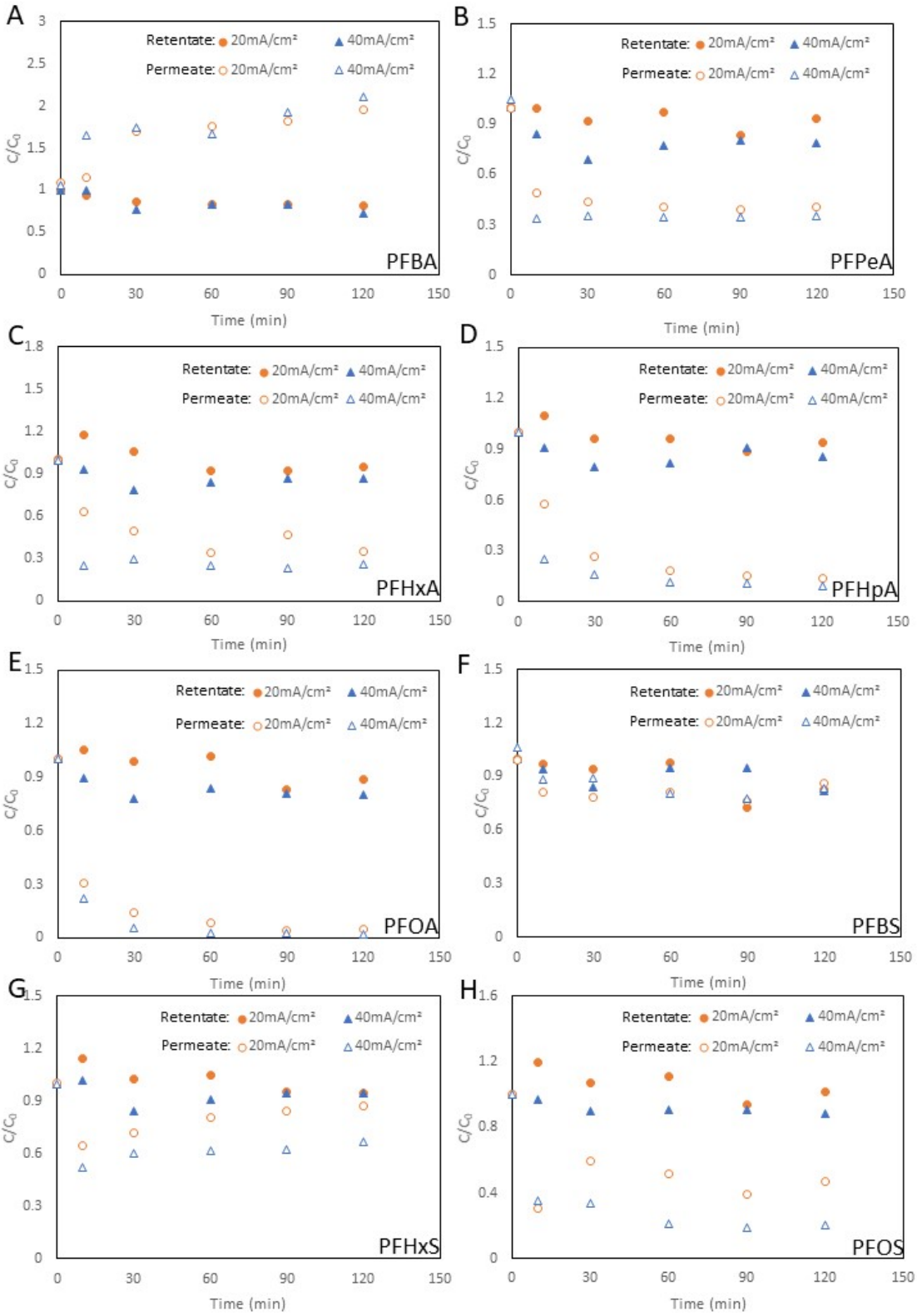

Figure 28. PFAA concentration in retentate and permeate during treatment of the PFAA mixture in 25-mM Na_2SO_4 by circular nano-Ti_4O_7 anode in cross-flow filtration mode at the current densities of 20 and 40 mA/cm^2. The permeate linear flow velocity was 0.02 cm/min.

4.3.3 Formation of chlorate and perchlorate

Chlorate and perchlorate were also monitored in the permeate and retentate in selected REM treatment systems. In one experiment, a 25-mM Na_2SO_4 solution containing the mixture PFAAs and 1.0-mM Cl^- were treated by nano-Ti_4O_7 REM at 40.0 mA/cm^2 and 0.02 cm/min permeate flow rate. It was found that the chlorate and perchlorate concentration in the permeate were 17.51 μM and 6.41 μM, respectively, and that in the retentate was zero for both chlorate and perchlorate. In another experiment, a 100-mM Na_2SO_4 solution containing the mixture PFAAs and 1.0-mM Cl^- were treated by Ebonex REM at 5.0 mA/cm^2 and 0.079 cm/min permeate flow rate. The chlorate and perchlorate concentration in the permeate was 9.69 μM and 0.20 μM, respectively, and that in the retentate was zero for chlorate and perchlorate. The formation of chlorate and perchlorate were much lower than that in batch reactor as in Figure 17. This is because of the much shorter residence time in the membrane during REM. Formation of chlorate and perchlorate and other disinfection byproducts (DBPs) is a known drawback for electrooxidation application in water treatment. The control of DBP formation during EO treatment may be achieved by regulating EO conditions (such as current density), adding scavengers of active chlorine and modifying the anode materials for reduced reactivity towards chloride, which is worth of further exploration.

4.4 Summary

We have evaluated two TSO anodes, circular nano-Ti_4O_7 and Ebonex, in a series of REM treatments operated in cross-flow filtration mode with PFOS solution. Effective PFOS degradation was found on both anodes, and the nano-Ti_4O_7 REM exhibited better performance than the Ebonex REM at the same anodic potential, and PFOS removal rate increased with increasing current density, consistent with that observed for batch reactor treatment. PFOS degradation rate was greatly higher in the REM treatment than in the batch reactor treatment for the same anode, as indicated by reaction rate constant normalized to the active electrochemical surface area. Accordingly, the electrical energy required to reduce one order of magnitude PFOS concentration (EE/O) by REM appeared to be much lower than that of the batch reactor treatment. The results indicated that REM enhanced EO efficiency not only by increasing substrate interphase mass transfer rates via convection facilitated dispersion but also making more anode surface available for reaction with the solution filtered through the REM.

The experiments of REM treatment on PFOS solution indicated that sorption of PFOS occurred on the micro- and nano-Ti_4O_7 materials when electric current was not applied, but the sorption did not occur on the Ebonex, while these sorption behaviors were absent in batch reactor experiments. Such sorption behaviors appeared to be related to the porous structures in the TSO ceramic membrane materials. PFOS sorption was the strongest on the micro-Ti_4O_7 material that has a significant fraction of nanopores while that was minimal in the nano-Ti_4O_7 material and absent in the Ebonex. The nanopores may facilitate micro-bubble formation when water containing the surface-active compound, PFOS, passing through the medium. Such sorption behavior was however not effective in a batch reactor operation, where the nanopores inside the medium was not available without FPOS solution filtered through. The strong sorption of PFOS or other PFAAs on the Ti_4O_7 material may be one phenomenon that can be exploited in REM treatment where PFAAs can be first concentrated on the anode via sorption and then degraded by EO, which is worth of further study.

Experiments were also conducted to evaluate REM treatments with the nano-Ti_4O_7 and Ebonex anode on the mixture PFAAs, including PFBA, PFPeA, PFHxA, PFHpA, PFOA, PFBS, PFHxS

and PFOS. In general, the long-chain PFAA degraded more effectively than the shorter chain ones. The order of the degradation rate constants for the PFAAs differ between the REM and the batch reactor treatments for both anodes, with the degradation of PFCAs faster than that of PFSAs in REM as opposed to the batch reactor treatment. The order of PFAA degradation rate constants varied between the REM and the batch reactor treatments, likely because the microporous structure within the TSO membranes that were made available during REM cross-flow filtration operation differs from that on the surface only of which was available for the batch reactor treatments.

Chlorate and perchlorate were formed in the permeate during REM treatment of PFAA solutions in the presence of chloride, dependent on the applied current density, but their formation appeared to be at lower levels than that in batch reactor, probably because of the much shorter residence time in the membrane during REM. Control of chlorate and perchlorate formation by regulating EO conditions and other means is possible and worth of further study.

5 Publications and future plans

5.1 publications

Two papers have been published as a result of the support in part by this project, which are listed below. In addition, two more manuscripts are in the process of preparation.

Lin H., Niu J., Liang S., Wang C., Wang Y., Jin F., Luo Q., Chiang S-Y, Huang Q., 2018, Development of macroporous Magnéli phase Ti_4O_7 ceramic materials: As an efficient anode for mineralization of poly- and perfluoroalkyl substances, Chemical Engineering Journal, 354, 1058-1067.

Liang S., Pierce Jr. R., Lin H., Chiang S-Y, Huang Q., 2018, Electrochemical oxidation of PFOA and PFOS in concentrated waste streams, Remediation Journal, 28, 127-134.

Shi H., Wang Y., Pierce Jr. R., Huang Q. 2019, Degradation of perfluorooctanesulfonate by Magneli phase titanium suboxide reactive electrochemical membrane. In preparation.

Wang L., Lu J., Huang Q. 2019, Effects of chloride on electrochemical degradation of perfluorooctanesulfonate on Magnéli phase Ti_4O_7 and boron doped diamond anodes. In preparation.

5.2 Future research plans

The results of this project indicate the potential of Magneli phase titanium suboxide (TSO) ceramic materials for applications in EO treatment to degrade PFAS. The performance of the TSO anodes are dependent on the composition of the materials and their porous structures. Further improvement of the TSO materials may thus be achieved by modifications targeted on the compositions and the porous structures. Such modifications may be tailored towards enhancing the reactivity of TSO anode towards PFAS, particularly shorter chain PFAAs, and simultaneously reducing its reactivity towards chloride to mitigate the formation of disinfection byproducts.

Modification of TSO compositions can be achieved by doping with elements such as cerium, bismuth and tin that can adjust the electrochemical reactivity by regulating electron transfer and interphase interactions. Two ways can be used for doping; one involves sintering of the doped elements mixed with Ti_4O_7, while the other uses pulsed laser deposition (PLS). For the sintering method, the anode porous structure can be adjusted by using different binder, bubble agents and granulation processes, while for PLS, pre-made ceramic membranes of different porous structure can be used as templates.

In addition to modification of the TSO materials, the other major direction for further research is improvement of the reactor and operation designs. For example, the TSO materials of abundant nanopores may facilitate effective PFAA adsorption that can be combined with EO treatment for enhanced performance. Such treatment would also mitigate DBP formation because chloride is not adsorbed and concentrated along with the PFAAs. Novel reactors may also be adopted using solid electrolytes to deal with contaminated water having low conductivities.

6 References

Azizi, O., Hubler, D., Schrader, G., Farrell, J. and Chaplin, B.P. (2011) Mechanism of Perchlorate Formation on Boron-Doped Diamond Film Anodes. Environmental Science & Technology 45(24), 10582-10590.

Barazesh, J.M., Prasse, C. and Sedlak, D.L. (2016) Electrochemical Transformation of Trace Organic Contaminants in the Presence of Halide and Carbonate Ions. Environmental Science & Technology 50(18), 10143-10152.

Donaghue, A. and Chaplin, B.P. (2013) Effect of Select Organic Compounds on Perchlorate Formation at Boron-doped Diamond Film Anodes. Environmental Science & Technology 47(21), 12391-12399.

Kapałka, A., Fóti, G. and Comninellis, C. (2008) Kinetic modelling of the electrochemical mineralization of organic pollutants for wastewater treatment. Journal of Applied Electrochemistry 38(1), 7-16.

Li, K., Eres, G., Howe, J., Chuang, Y.-J., Li, X., Gu, Z., Zhang, L., Xie, S. and Pan, Z. (2013) Self-Assembly of Graphene on Carbon Nanotube Surfaces. Scientific Reports 3, 2353.

Liang, S.R.D.P.L., Hui; Chiang, Sheau-Yun; Huang,Qingguo (2018) Electrochemical oxidation of PFOA and PFOS in concentrated waste streams. Remediation Journal 28(2), 127-134.

Lin, H., Niu, J., Liang, S., Wang, C., Wang, Y., Jin, F., Luo, Q. and Huang, Q. (2018) Development of macroporous Magnéli phase Ti4O7 ceramic materials: As an efficient anode for mineralization of poly- and perfluoroalkyl substances. Chemical Engineering Journal 354, 1058-1067.

Lin, Z., Yao, W., Wang, Y., Yu, G., Deng, S., Huang, J. and Wang, B. (2016) Perchlorate formation during the electro-peroxone treatment of chloride-containing water: Effects of operational parameters and control strategies. Water Research 88, 691-702.

Lindstrom, A.B., Strynar, M.J. and Libelo, E.L. (2011) Polyfluorinated Compounds: Past, Present, and Future. Environmental Science & Technology 45(19), 7954-7961.

Luo, Q., Yan, X., Lu, J. and Huang, Q. (2018) Perfluorooctanesulfonate Degrades in a Laccase-Mediator System. Environmental Science & Technology 52(18), 10617-10626.

Niu, J., Lin, H., Xu, J., Wu, H. and Li, Y. (2012) Electrochemical Mineralization of Perfluorocarboxylic Acids (PFCAs) by Ce-Doped Modified Porous Nanocrystalline PbO2 Film Electrode. Environmental Science & Technology 46(18), 10191-10198.

Park, H., Vecitis, C.D. and Hoffmann, M.R. (2009) Electrochemical Water Splitting Coupled with Organic Compound Oxidation: The Role of Active Chlorine Species. The Journal of Physical Chemistry C 113(18), 7935-7945.

Schaefer, C.E., Andaya, C., Urtiaga, A., McKenzie, E.R. and Higgins, C.P. (2015) Electrochemical treatment of perfluorooctanoic acid (PFOA) and perfluorooctane sulfonic acid (PFOS) in groundwater impacted by aqueous film forming foams (AFFFs). Journal of Hazardous Materials 295, 170-175.

Schmidt, L.D. (2005) The engineering of chemical reactions, Oxford University Press, New York.

Yang, K., Lin, H., Liang, S., Xie, R., Lv, S., Niu, J., Chen, J. and Hu, Y. (2018) A reactive electrochemical filter system with an excellent penetration flux porous Ti/SnO2–Sb filter for efficient contaminant removal from water. RSC Advances 8(25), 13933-13944.

Yu, Q., Zhang, R., Deng, S., Huang, J. and Yu, G. (2009) Sorption of perfluorooctane sulfonate and perfluorooctanoate on activated carbons and resin: Kinetic and isotherm study. Water Research 43(4), 1150-1158.

Zaky, A.M. and Chaplin, B.P. (2013) Porous Substoichiometric TiO2 Anodes as Reactive Electrochemical Membranes for Water Treatment. Environmental Science & Technology 47(12), 6554-6563.

Zhi, J.-F., Wang, H.-B., Nakashima, T., Rao, T.N. and Fujishima, A. (2003) Electrochemical Incineration of Organic Pollutants on Boron-Doped Diamond Electrode. Evidence for Direct Electrochemical Oxidation Pathway. The Journal of Physical Chemistry B 107(48), 13389-13395.

Appendix 1

Table 1 Acronym List

Abbreviation	Explanation
PFOS	Perfluorooctanesulfonic acid
PFAS	Per- and polyfluoroalkyl substances
PFAAs	Perfluoroalkyl acids
EO	Electrooxidation
DET	Direct electron transfer
XRD	X ray diffraction
TCE	Trichloroethylene
TSO	Porous titanium suboxide
REM	Reactive electrochemical membrane
CoCs	Contaminants of concern
PFBA	Perfluoro-n-butanoic acid
PFPeA	Perfluoro-n-pentanoic acid
PFHxA	Perfluoro-n-hexanoic acid
PFHpA	Perfluoro-n-heptanoic acid
PFOA	Perfluoro-n-octanoic acid
PFBS	Perfluoro-1-butanesulfonate
PFHxS	Perfluoro-1-hexanesulfonate
M8PFOS	Perfluoro-1-[$^{13}C_8$]-octane sulfonate
MRM	Multiple reaction monitoring
EE/O	Electrical efficiency per log order reduction
L-PFOS	Linear perfluorooctanesulfonic acid
B-PFOS	Branched perfluorooctanesulfonic acid

k_{SA}	Surface area normalized reaction rate
IC	Ion chromatography
dF	Defluorination ratio
ISE	Fluoride ion selective electrode
LOQs	Limits of quantifications
PFCAs	Perfluoroalkyl carboxylic aids
PFSAs	Perfluoroalkanesulfonic acids
PFCs	Perfluorinated compounds

Appendix 2

Table 2 Limits of quantifications (LOQs)

(no SPE concentration factor considered)

No.	Compound Name	LOQ (ppb)
1	PFBA	2.6
2	PFPeA	2.8
3	PFBS	1.6
4	PFHxA	1.5
5	PFHpA	1.5
6	PFHxS	2.4
7	PFOA	1.4
8	PFOS	2.7

Appendix 3

Table 3 Batch experiments on PFOS degradation

Number #	Electrolyte	Reactor Setup	Reaction solution volume (mL)	Anode material	Current density (mA/cm^2)	k_{SA} for L-PFOS (m/s)	Standard diviation of k_{SA} for L-PFOS	k_{SA} for B-PFOS (m/s)	Standard deviation of k_{SA} for B-PFOS
1	100mM Na_2SO_4	Reactor Setup I	50	Circular nano-Ti_4O_7	2.5	7.28×10^{-6}	5.09×10^{-7}	7.12×10^{-6}	5.98×10^{-7}
2					4.0	9.14×10^{-6}	6.44×10^{-7}	9.34×10^{-6}	6.69×10^{-7}
3					5.0	2.14×10^{-5}	3.58×10^{-6}	2.25×10^{-5}	1.59×10^{-6}
4					10.0	5.45×10^{-5}	8.97×10^{-7}	5.56×10^{-5}	2.65×10^{-6}
5					15.0	1.19×10^{-4}	1.61×10^{-6}	1.23×10^{-4}	3.33×10^{-7}
6					20.0	2.12×10^{-4}	8.62×10^{-6}	2.23×10^{-4}	4.50×10^{-6}
7					40.0	3.88×10^{-4}	1.40×10^{-5}	4.04×10^{-4}	7.41×10^{-6}
8					60.0	6.07×10^{-4}	5.56×10^{-5}	5.66×10^{-4}	2.07×10^{-5}
9					90.0	7.56×10^{-4}	3.88×10^{-5}	6.43×10^{-4}	2.83×10^{-5}
10					120.0	7.63×10^{-4}	3.76×10^{-5}	6.44×10^{-4}	7.46×10^{-5}
11					150.0	1.30×10^{-3}	1.45×10^{-4}	1.14×10^{-3}	6.95×10^{-4}
12					180.0	1.40×10^{-3}	2.58×10^{-4}	1.37×10^{-3}	4.20×10^{-5}

13					210.0	1.28×10^{-3}	1.31×10^{-4}	1.39×10^{-3}	1.41×10^{-4}
14				Circular micro-Ti_4O_7	2.5	3.98×10^{-6}	4.09×10^{-8}	6.25×10^{-6}	5.24×10^{-8}
15					4.0	1.24×10^{-5}	8.53×10^{-8}	1.34×10^{-5}	1.71×10^{-8}
16					5.0	1.42×10^{-5}	2.76×10^{-8}	1.48×10^{-5}	1.07×10^{-6}
17					10.0	6.87×10^{-5}	1.00×10^{-5}	6.62×10^{-5}	7.33×10^{-6}
18					15.0	7.77×10^{-5}	1.92×10^{-6}	7.97×10^{-5}	1.28×10^{-6}
19					20.0	1.06×10^{-4}	1.35×10^{-6}	1.07×10^{-4}	2.59×10^{-5}
20					40.0	4.45×10^{-4}	3.62×10^{-7}	4.33×10^{-4}	6.37×10^{-6}
21					60.0	7.41×10^{-4}	1.18×10^{-5}	7.51×10^{-4}	1.38×10^{-4}
22					90.0	8.41×10^{-4}	2.25×10^{-5}	7.40×10^{-4}	8.28×10^{-5}
23					120.0	8.82×10^{-4}	2.26×10^{-5}	7.80×10^{-4}	1.26×10^{-4}
24					150.0	8.95×10^{-4}	3.15×10^{-6}	1.06×10^{-3}	3.20×10^{-5}
25					180.0	1.42×10^{-3}	2.25×10^{-4}	1.37×10^{-3}	6.85×10^{-8}
26					210.0	2.13×10^{-3}	7.67×10^{-4}	1.99×10^{-3}	2.69×10^{-5}
27		Reactor Setup IV	250	Ebonex	0.5	0	0.0000	0	0.0000
28					1.0	1.90×10^{-6}	9.48×10^{-7}	1.42×10^{-6}	1.04×10^{-6}
29					2.5	8.78×10^{-6}	1.04×10^{-6}	7.69×10^{-6}	2.19×10^{-6}
30					4.0	1.96×10^{-5}	2.84×10^{-6}	1.38×10^{-5}	1.90×10^{-6}

31					7.0	3.36×10^{-5}	4.58×10^{-6}	2.49×10^{-5}	4.72×10^{-6}
32					10.0	4.62×10^{-5}	7.30×10^{-6}	3.79×10^{-5}	1.31×10^{-6}
33					15.0	6.37×10^{-5}	4.27×10^{-6}	5.09×10^{-5}	3.48×10^{-6}
34					25.0	6.73×10^{-5}	5.86×10^{-6}	6.08×10^{-5}	5.15×10^{-6}
35					30.0	7.64×10^{-5}	4.33×10^{-6}	7.96×10^{-5}	8.22×10^{-6}
36					40.0	8.30×10^{-5}	4.08×10^{-6}	8.52×10^{-5}	3.84×10^{-6}
37					50.0	9.98×10^{-5}	2.41×10^{-6}	1.20×10^{-4}	4.81×10^{-6}
38					70.0	1.21×10^{-4}	7.73×10^{-6}	1.42×10^{-4}	7.2×10^{-6}
39					90.0	1.26×10^{-4}	6.83×10^{-6}	1.44×10^{-4}	7.89×10^{-6}
40					110.0	1.27×10^{-4}	7.70×10^{-6}	1.44×10^{-4}	8.63×10^{-6}
41		Reactor Setup III	200	Rectangular nano-Ti_4O_7	5.0	5.10×10^{-5}	7.61×10^{-6}		
42					10.0	1.43×10^{-4}	2.93×10^{-6}	1.53×10^{-4}	1.50×10^{-6}
43					20.0	2.08×10^{-4}	1.20×10^{-5}	2.30×10^{-4}	1.29×10^{-5}
44					40.0	3.43×10^{-4}	6.95×10^{-6}	3.64×10^{-4}	7.72×10^{-6}
45	10mM Na_2SO_4	Reactor Setup II	100	Rectangular nano-Ti_4O_7	10.0	7.80×10^{-5}	1.41×10^{-6}		
46	25mM Na_2SO_4					7.55×10^{-5}	1.16×10^{-6}		

47	100mM $NaNO_3$					5.36×10^{-5}	2.48×10^{-6}		
48	100mM Na_2SO_4					5.55×10^{-5}	1.45×10^{-6}		
49	100mM $NaClO_4$					5.94×10^{-5}	1.74×10^{-6}		
50	50mM H_2SO_4	Reactor Setup III	200		5.0	3.43×10^{-5}	3.27×10^{-6}		
51	100mM NaOH					4.73×10^{-5}	1.16×10^{-6}		
52	100mM Phosphate buffer					4.74×10^{-5}	3.61×10^{-6}		
53	100mM Na_2SO_4	Reactor Setup I	50	Circular graphene-coated micro-Ti_4O_7	20.0	1.12×10^{-4}	1.21×10^{-6}		
54	100mM Na_2SO_4 Without TCE	Reactor Setup III	200	Rectangular nano-Ti_4O_7	5.0	6.84×10^{-5}	4.75×10^{-6}	6.85×10^{-5}	1.37×10^{-5}
55	100mM Na_2SO_4					7.50×10^{-5}	7.55×10^{-7}	1.41×10^{-4}	2.56×10^{-5}

	+5ppm TCE								
56	100mM Na_2SO_4 +10ppm TCE					9.44×10^{-5}	7.65×10^{-6}	7.30×10^{-5}	5.45×10^{-6}
57	100mM Na_2SO_4 +20ppm TCE					6.50×10^{-5}	8.46×10^{-6}	$5.59\times10^{-}$	1.00×10^{-6}
58	100mM Na_2SO_4 +50ppm TCE					5.50×10^{-5}	7.57×10^{-6}	5.56×10^{-5}	3.68×10^{-6}

Appendix 4

Table 4 Batch experiments on PFAS mixture degradation

Number #	Electrolyte	Reactor Setup	Anode material	Reaction solution volume (mL)	Current density (mA/cm^2)	Component	k_{SA} (m/s)	Standard deviation of k_{SA}
1	100 mM Na_2SO_4	Reactor Setup III	Rectangular nano-Ti_4O_7	200	1.0	PFBA	3.33×10^{-7}	3.52×10^{-8}
						PFPeA	7.17×10^{-7}	5.70×10^{-8}
						PFHxA	7.17×10^{-7}	5.43×10^{-8}
						PFHpA	1.00×10^{-6}	3.33×10^{-8}
						PFOA	6.33×10^{-6}	1.52×10^{-7}
						L-PFBS	5.67×10^{-7}	4.12×10^{-8}
						L-PFHxS	3.17×10^{-6}	2.82×10^{-8}
						L-PFOS	1.37×10^{-5}	3.10×10^{-7}
2					2.0	PFBA	3.33×10^{-7}	3.98×10^{-8}
						PFPeA	3.67×10^{-7}	2.53×10^{-8}
						PFHxA	7.17×10^{-7}	2.30×10^{-8}
						PFHpA	3.28×10^{-6}	5.33×10^{-8}
						PFOA	7.50×10^{-6}	3.43×10^{-7}

						L-PFBS	7.67×10^{-7}	3.85×10^{-8}
						L-PFHxS	5.33×10^{-6}	5.53×10^{-8}
						L-PFOS	2.23×10^{-5}	9.10×10^{-7}
3					5.0	PFBA	4.30×10^{-7}	4.65×10^{-8}
						PFPeA	7.17×10^{-7}	3.07×10^{-8}
						PFHxA	2.00×10^{-6}	2.40×10^{-8}
						PFHpA	5.83×10^{-6}	1.22×10^{-7}
						PFOA	2.45×10^{-5}	2.73×10^{-7}
						L-PFBS	8.12×10^{-7}	2.65×10^{-8}
						L-PFHxS	1.50×10^{-5}	1.21×10^{-6}
						L-PFOS	3.83×10^{-5}	2.32×10^{-6}
4					7.5	PFBA	6.33×10^{-7}	4.67×10^{-8}
						PFPeA	2.33×10^{-7}	1.48×10^{-7}
						PFHxA	5.02×10^{-6}	1.70×10^{-7}
						PFHpA	2.87×10^{-6}	9.47×10^{-7}
						PFOA	9.78×10^{-5}	4.27×10^{-6}
						L-PFBS	3.38×10^{-6}	6.77×10^{-8}
						L-PFHxS	7.17×10^{-5}	2.85×10^{-6}

						L-PFOS	1.17×10^{-4}	3.50×10^{-6}
5					10.0	PFBA	6.69×10^{-7}	3.43×10^{-8}
						PFPeA	2.20×10^{-6}	6.33×10^{-8}
						PFHxA	6.07×10^{-6}	8.23×10^{-8}
						PFHpA	5.17×10^{-5}	1.94×10^{-6}
						PFOA	1.00×10^{-4}	4.24×10^{-6}
						L-PFBS	2.72×10^{-6}	6.50×10^{-8}
						L-PFHxS	9.55×10^{-5}	6.55×10^{-6}
						L-PFOS	1.15×10^{-4}	5.03×10^{-6}
6					15.0	PFBA	1.37×10^{-6}	5.02×10^{-8}
						PFPeA	2.62×10^{-6}	2.92×10^{-8}
						PFHxA	9.50×10^{-6}	1.66×10^{-7}
						PFHpA	5.17×10^{-5}	1.70×10^{-6}
						PFOA	1.28×10^{-4}	5.50×10^{-6}
						L-PFBS	7.33×10^{-6}	2.08×10^{-7}
						L-PFHxS	1.17×10^{-4}	9.87×10^{-21}
						L-PFOS	1.33×10^{-4}	5.33×10^{-6}
7			Ebonex	100	5.0	PFBA	1.52×10^{-6}	4.57×10^{-8}

						PFPeA	2.10×10^{-6}	4.75×10^{-7}
						PFHxA	3.28×10^{-6}	3.75×10^{-7}
						PFHpA	1.26×10^{-5}	3.43×10^{-7}
						PFOA	2.59×10^{-5}	9.49×10^{-10}
						L-PFBS	1.27×10^{-6}	2.49×10^{-7}
						L-PFHxS	1.40×10^{-5}	3.06×10^{-7}
						L-PFOS	4.01×10^{-5}	4.90×10^{-7}
					10.0	PFBA	2.88×10^{-6}	5.12×10^{-7}
						PFPeA	2.56×10^{-6}	5.58×10^{-7}
						PFHxA	3.31×10^{-6}	3.26×10^{-7}
						PFHpA	1.34×10^{-5}	4.49×10^{-7}
						PFOA	2.97×10^{-5}	2.81×10^{-7}
						L-PFBS	1.27×10^{-6}	1.00×10^{-7}
						L-PFHxS	1.95×10^{-5}	9.41×10^{-7}
						L-PFOS	5.20×10^{-5}	8.21×10^{-8}
9					15.0	PFBA	3.41×10^{-6}	1.42×10^{-6}
						PFPeA	3.95×10^{-6}	3.34×10^{-7}
						PFHxA	1.16×10^{-5}	6.32×10^{-7}

						PFHpA	5.07×10^{-5}	5.22×10^{-6}
						PFOA	7.72×10^{-5}	6.30×10^{-7}
						L-PFBS	3.95×10^{-6}	2.85×10^{-7}
						L-PFHxS	5.87×10^{-5}	7.04×10^{-6}
						L-PFOS	8.05×10^{-5}	8.51×10^{-6}
10					20.0	PFBA	3.84×10^{-6}	4.81×10^{-8}
						PFPeA	3.60×10^{-6}	1.98×10^{-7}
						PFHxA	8.31×10^{-6}	1.48×10^{-7}
						PFHpA	3.57×10^{-5}	7.51×10^{-6}
						PFOA	8.06×10^{-5}	5.37×10^{-7}
						L-PFBS	3.20×10^{-6}	2.84×10^{-7}
						L-PFHxS	5.25×10^{-5}	7.49×10^{-6}
						L-PFOS	8.57×10^{-5}	6.06×10^{-6}
11	100mM Na_2SO_4	Reactor Setup III	Rectangular nano-Ti_4O_7	200	5.0	PFBA	2.17×10^{-7}	2.50×10^{-8}
12						PFPeA	3.67×10^{-7}	1.47×10^{-8}
13						PFHxA	3.00×10^{-6}	3.52×10^{-8}
14						PFHpA	7.50×10^{-6}	4.22×10^{-8}
15						PFOA	3.52×10^{-5}	3.29×10^{-7}

16						L-PFBS	1.05×10^{-6}	4.72×10^{-8}
17						L-PFHxS	3.00×10^{-6}	9.84×10^{-7}
18						L-PFOS	5.10×10^{-5}	6.14×10^{-6}

Appendix 5

Table 5 Cross-flow experiments on PFOS degradation

Number #	Electrolyte	Reactor Setup	Anode material	Back Pressure (psi)	Flow rate (cm/min)	Current density (mA/cm^2)	k (/s) for L-PFOS	Standard deviation of k for L-PFOS	k (/s) for B-PFOS	Standard deviation of k for B-PFOS
1	100mM Na_2SO_4	Reactor setup for tubular REM	Ebonex	10	0.079	0.2	0.0000	0.0000	0.0000	0.0000
2						0.5	0.0035	0.0002	0.0023	0.0006
3						1.0	0.0093	0.0005	0.0121	0.0001
4						1.2	0.0104	0.0019	0.0145	0.0026
5						1.5	0.0243	0.0060	0.0249	0.0036
6						1.8	0.0301	0.0023	0.0335	0.0047
7						2.1	0.0503	0.0039	0.0538	0.0006
8						2.5	0.0862	0.0058	0.0844	0.0027
9						4.0	0.0868	0.0048	0.0885	0.0027
10						7.0	0.0862	0.0019	0.0879	0.0004
11				18	0.14	1.0	0.0081	0.0039	0.0075	0.0006
12				7	0.056		0.0093	0.0021	0.0052	0.0002
13				3	0.024		0.0064	0.0002	0.0029	0.0002

14	25mM Na_2SO_4	Reactor setup for circular REM	Circular nano-Ti_4O_7	0.01	0.02	10.0	0.0492	0.0082	0.0504	0.0097
15						20.0	0.1687	0.0200	0.1531	0.0302
16						40.0	0.1958	0.0144	0.2122	0.0158

Appendix 6

Table 6 Cross-flow experiments on PFAA mixture degradation

Number #	Electrolyte	Reactor Setup	Anode material	Back Pressure (psi)	Flow rate (cm/min)	Current density (mA/cm^2)	Component	k (/s)	Standard deviation of k
1	25 mM Na_2SO_4	Reactor setup for circular REM	Circular nano-Ti_4O_7	0.01	0.02	20.0	PFBA	-0.0728	0.0066
							PFPeA	0.1102	0.0033
							PFHxA	0.1088	0.0210
							PFHpA	0.2068	0.0184
							PFOA	0.3138	0.0481
							L-PFBS	0.0266	0.0075
							L-PFHxS	0.0261	0.0049
							L-PFOS	0.0971	0.0167
2						40.0	PFBA	-0.0740	0.0127
							PFPeA	0.1312	0.0021
							PFHxA	0.1675	0.0130
							PFHpA	0.2598	0.0271
							PFOA	0.4200	0.0455

							L-PFBS	0.0217	0.0073
							L-PFHxS	0.0612	0.0049
							L-PFOS	0.1786	0.0327
3		*Reactor setup for tubular REM*	Ebonex	10	0.079	5.0	PFBA	-0.0064	0.0029
							PFPeA	0.0197	0.0029
							PFHxA	0.0440	0.0069
							PFHpA	0.0341	0.0046
							PFOA	0.0393	0.0069
							L-PFBS	0.0110	0.0029
							L-PFHxS	0.0289	0.0040
							L-PFOS	0.0388	0.0081